Master's thesis

NTNU
Norwegian University of Science and Technology
Faculty of Engineering
Department of Structural Engineering

Håvar Johan Junker
Vegar Tviberg

Finite element modeling of porcine mitral valve apparatus using realistic annular motion from sono-crystal measurements and corresponding echocardiography

Master's thesis in Mechanical Engineering
Supervisor: Assoc. Prof. Victorien E. Prot
June 2020

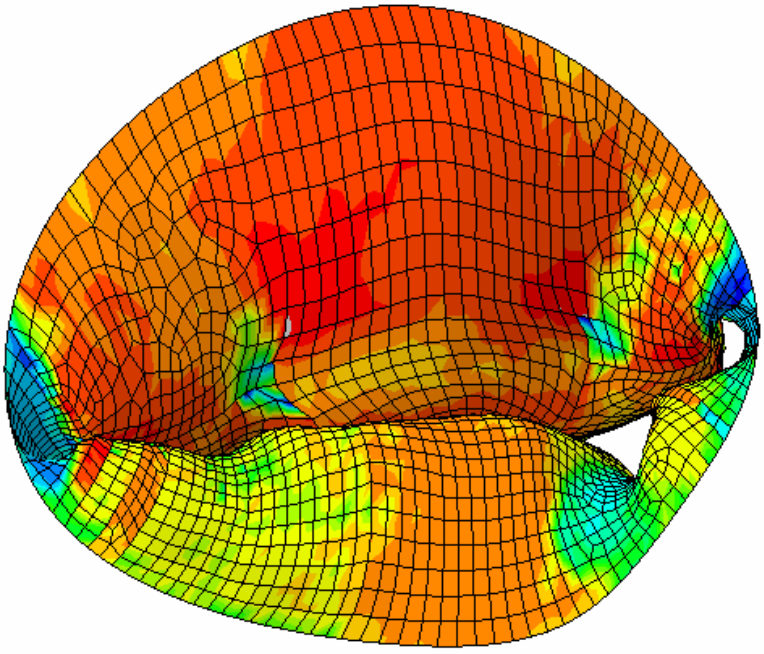

NTNU
Kunnskap for en bedre verden

Håvar Johan Junker
Vegar Tviberg

Finite element modeling of porcine mitral valve apparatus using realistic annular motion from sono-crystal measurements and corresponding echocardiography

Master's thesis in Mechanical Engineering
Supervisor: Assoc. Prof. Victorien E. Prot
June 2020

Norwegian University of Science and Technology
Faculty of Engineering
Department of Structural Engineering

NTNU

Kunnskap for ei betre verd

Department of Structural Engineering
Faculty of Engineering
NTNU – Norwegian University of Science and Technology

ACCESSIBILITY

OPEN

MASTER THESIS 2020

SUBJECT AREA: Applied Mechanics (Biomechanics)	DATE: 08.06.2020	NO. OF PAGES: 88

TITLE:

Finite element modeling of porcine mitral valve apparatus using realistic annular motion from sono-crystal measurements and corresponding echocardiography

BY:

Håvar Johan Junker

Vegar Tviberg

SUMMARY:

A fundamental understanding of the mitral valve (MV) dynamics is needed to predict the long-term outcome of its related diseases. Numerical mechanical analysis, herein the finite element method (FEM), can be used to assess the local and regional deformations of the MV. This method has proven a valuable tool in diagnostics and clinical research. The aim of this study was to investigate the influence of annular motion during atrial contraction on the MV closure of a porcine heart by generating a hyperelastic FEM-model. Using corresponding *in vivo* sono-crystal and 3D echocardiographic measurements, the influence of annular motion was quantified by modifying the dynamic boundary conditions of the model. The subsequent mechanical assessment showed that the model was sensitive to the accuracy of the boundary conditions, and that an implementation of residual strains in the model in necessary to better align with the *in vivo* state of the MV. Additionally, the modification of annular motion had little effect on the MV closure mechanism. Ultimately, it is concluded that the modified annular motion is not solely capable of hindering MV closure. However, experimental data with higher resolution is necessary to validate the results.

RESPONSIBLE TEACHER:

SUPERVISOR: Assoc. Prof. Victorien E. Prot

CARRIED OUT AT: NTNU

Abstract

A fundamental understanding of the mitral valve (MV) dynamics is needed to predict the long-term outcome of its related diseases. Numerical mechanical analysis, herein the finite element method (FEM), can be used to assess the local and regional deformations of the MV. This method has proven a valuable tool in diagnostics and clinical research. The aim of this study was to investigate the influence of annular motion during atrial contraction on the MV closure of a porcine heart by generating a hyperelastic FEM-model. Using corresponding *in vivo* sono-crystal and 3D echocardiographic measurements, the influence of annular motion was quantified by modifying the dynamic boundary conditions of the model. The subsequent mechanical assessment showed that the model was sensitive to the accuracy of the boundary conditions, and that an implementation of residual strains in the model in necessary to better align with the *in vivo* state of the MV. Additionally, the modification of annular motion had little effect on the MV closure mechanism. Ultimately, it is concluded that the modified annular motion is not solely capable of hindering MV closure. However, experimental data with higher resolution is necessary to validate the results.

Keywords: Mitral valve, annulus motion, atrial contraction, FEM, sono-crystal

Sammendrag

En grundig og nøyaktig forståelse av mitralklaffens dynamikk er nødvendig og etterspurt for å utvikle gode prognoser for langtidsvirkningene av mitralklaffdefekter. Numeriske beregningsmetoder, deriblant elementmetoden ("FEM"), kan brukes til å beregne de lokale deformasjonene i mitralklaffen. Dette har vist seg å være et verdifullt hjelpemiddel i klinisk sammenheng. Målet med denne studien var å utvikle en elementmetodemodell av mitralklaffen til et svinehjerte, basert på samsvarende piezoelektriske krystallmålinger og ultralydbilder tatt i et levende svinehjerte. Videre ble effekten av atriell kontraksjon på mitralklaffens globale dynamikk forsøkt kvantifisert ved hjelp av modifiserte randbetingelser. Den påfølgende evalueringen viste at modellen var sensitiv overfor nøyaktigheten til randbetingelsene. Videre funn indikerte at residualtøyninger i framtiden burde tas hensyn til for tilnærme den sanne tilstanden til klaffen bedre. De modifiserte randbetingelsene viste liten effekt på klaffens lukkemekanisme, og det konkluderes tilslutt med at denne typen randbevegelse i seg selv ikke er i stand til å hindre lukkingen av mitralklaffen. For å være i stand til å validere funnene i denne studien konkluderes det med at bedre eksperimentelle målinger må innhentes.

Stikkord: Mitralklaffen, annulusbevegelse, atriell kontraksjon, elementmetoden, piezoelektriske krystaller

Assignment

The mitral valve is a thin walled complex connective tissue structure located between the left atrium and left ventricle preventing the blood from flowing back into the atrium when the ventricle contracts. The mitral apparatus consists of two leaflets (named anterior and posterior) attached to the annulus, which is an ill-defined line between the left atrium and the left ventricle. The mitral leaflets are connected to a network of chordae tendinae further attached to the papillary muscles which originates from the left ventricular wall. The normal function of the mitral valve depends on the coordinated actions of different anatomical parts: the left atrium, the mitral annulus, the mitral leaflets, the chordae tendinae, the papillary muscles and the left ventricle. Numerical mechanical analysis of the mitral valve can be used to assess mechanical stresses and global and local deformations in the different components of the valve. The finite element (FE) method is one example of these numerical approaches.

Accurate geometry, material behaviors and boundary conditions are of crucial importance to perform reliable FE analyses. Furthermore, it is well known that the non-planar mitral annulus undergoes large deformations during the cardiac cycle. Therefore, the motion of the annulus needs to be prescribed to FE models of the mitral apparatus.

The primary goal of this project is to establish finite element models of a porcine mitral valve using realistic annular motion obtained from sono-crystal measurements, corresponding 3D echocardiography and blood pressure history in order to perform dynamic analysis of the mitral valve apparatus during the cardiac cycle. The dynamic deformations of the annulus will be implemented as displacement boundary conditions into the FE code ABAQUS. In addition, the resultant force carried by the papillary muscles and the mitral annulus ring will be assessed.

Sono-crystal data show that atrial contraction, which occurs just before ventricular systole, induces complex deformations of the mitral annulus while the mitral valve is still open. The influence of atrial contraction on mitral valve mechanics has been discussed in a previous study but is still not fully understood. Hence, a secondary goal of this project is to establish a numerical protocol to test the role of atrial contraction on mitral valve closure.

Acknowledgements

First and foremost, we would like to express our deepest gratitudes to Assoc. Prof. Victorien E. Prot for his professional guidance and enthusiastic encouragement from the very beginning of this project. His positive attitude and humor motivated us to work hard.

Moreover, we are deeply thankful to Dr.med Stig Urheim for providing us with the data sets used in this study, as well as his willingness to answer our questions regarding cardiac anatomy. It has been greatly appreciated.

We want to thank Hans Martin Aguilera for providing his unique expertise in explicit analysis in ABAQUS, which greatly increased the progress of our work. Furthermore, we wish to acknowledge Mohammad Javad Sadeghinia for providing us with literature, which significantly increased the quality of this thesis.

Last, but not least, we wish to thank our colleagues at NTNU for a motivating and encouraging work environment.

I want to express gratitude to my family and friends for always cheering on me throughout the process of writing this thesis. Most of all, I want to thank my Andrine Lodgaard for eternal support and bringing joy to the prolonged writing sessions.

V. Tviberg

I would like to acknowledge my closest family and friends for their continuous support throughout my years of studies. Moreover, I wish to thank Frida, Nora and Jardar Junker who have kept my spirits high. Lastly, I am deeply grateful to my Louise Victoria Larsson for her substantial effort in the proofreading of this thesis. It has certainly been greatly appreciated.

H. J. Junker

Contents

List of Figures

List of Tables

Acronyms

AC Atrial contraction

AL Anterolateral

ALC Anterolateral commisure

AML Anterior mitral leaflet

BC Boundary condition

CW commissure width

ECG Electrocardiogram

ECM Extracellular matrix

EDV End diastolic volume

ESV End systolic volume

FEM Finite element method

GUI Graphical user interface

HVD Heart valve diseases

LA Left atrium

LV Left ventricle

LVP Left ventricle pressure

MA Mitral annulus

MR Mitral regurgitation

MV Mitral valve

PM Posteromedial

PMC Posteromedial commisure

PML Posterior mitral leaflet

SL Septal-lateral length

US Ultrasound

VIC Valve interstitial cell

1. Introduction

The epidemiology of heart valve diseases (HVD) has changed rapidly over the last century [1]. Whereas a majority of the morbidity related to HVD in low-income countries are still related to rheumatic heart disease inheriting from bacterial infections, high-income countries have seen a drastical increase in lifestyle-related HVD. This has been largely associated with the development of the health care system in high-income countries, which made it possible to tackle the aforementioned bacterial infections. [2] As age is one of the major risk factors in developing HVD, the globally increasing life expectancy is expected to vastly increase the clinical burden of HVD [3].

Although calcified aortic valve disease is the most important HVD in terms of mortality, population-based studies suggest that mitral regurgitation (MR) is the most prevalent form of mild or severe HVD [4]. MR manifests itself as the name suggests as regurgitative flow in the mitral valve (MV), one of the four valves in the human heart [5]. The MV is located between the left atrium (LA) and left ventricle (LV), in place to prevent regurgitative blood flow back into the LA during ventricular contraction [6]. The MV apparatus is a complex structure comprised of various anatomical parts, fulfilling the role of the MV through highly coordinated actions.

A thorough understanding of the MV and its dynamics is needed in order to predict the long term effects of MR. Clinically, this has traditionally been done using medical imaging techniques such as ultrasound (US) and magnetic resonance [7, 8]. Eventually, computational biomechanics emerged as an invaluable tool in clinical research and diagnostics. More recently, the implementation of advanced numerical methods, such as the finite element method (FEM), have provided unique insights in the mechanical assessment of the MV in even patient specific studies [9]. Expanding the horizons of FEM, the current trend is to model the MV using hyperelastic material models [10, 11].

In order to simulate the MV dynamics, a set of dynamic boundary conditions (BCs) must be prescribed. Due to the complexity of the deformations, tracking of material points has proven difficult using US. In contrast, sonomicrometric crystals (hereafter: crystals) can be used to track the motion of certain material points with very high accuracy [12]. The technique is based on the transmittance of sound waves in between piezo-electric transducers. The transit time of the sound waves can then be used to locate the crystals relative to each other. Herein, parts of the BCs has been obtained in an *in vivo* study using sonomicrometry, allowing for a very accurate prescription of the BCs [13].

The functioning of the MV depends on several complex and interacting determinants [14]. The role of the atrial walls was highlighted nearly 200 years ago [15]. Since then, there has been a continuing controversy regarding the relative importance of atrial contraction (AC) on ventricular filling and MV closure [16]. Previous studies on the topic has been of clinical art, mainly focusing on quantifying the effects of AC using purely clinical metrics [17, 18]. In this study, the role of AC on the MV mechanics have been assessed by modifying the BCs of a hyperelastic FEM model of a porcine heart correspondingly. To the authors' knowledge, this is the first time the effects of AC on the MV apparatus have been assessed using FEM.

The thesis has been outlined as follows: First, the necessary anatomy and physiology of the human heart is presented, followed by a brief review of the different constituents of the MV apparatus. Thereafter, a section on the mechanobiology of the MV leaflets follows, immediately linked to their highly nonlinear material behaviour.

The MV apparatus is then viewed in context of a continuum mechanical framework. The necessary background theory of nonlinear continuum mechanics is presented, as well as current trends of constitutive modelling. Thereafter, the FEM-modelling of the MV apparatus and implementation of dynamic BCs is described.

The results are then presented. As the relation between two independent dynamic systems was found to heavily affect the subsequent results, their respective dynamics are quantified and related. Thereafter, the results from the FEM-analysis are presented with increasing complexity with respect to BCs. Thereafter, the results are discussed and viewed in context of current findings in computational biomechanics. Ultimately, a few concluding remarks regarding the validity and future possibilities of this study have been made.

2. Aims and objectives

The scientific aim of this project was to assess the influence of AC on the MV closure mechanism through a modification of the BCs. It was achieved by a systematic conduction of the following objectives:

- A comprehensive literature review focusing on the anatomy of the different constituents of the MV apparatus
- An investigation of the mechanobiology of the MV apparatus to increase the understanding regarding its mechanical behaviour
- The generation of a hyperelastic FEM-model of the MV apparatus, involving dynamic BCs obtained from two different coordinate frames
- A modification of the BCs to investigate the influence of annular motion during AC on the MV closure mechanism

3. Theoretical background

3.1 The human heart

The heart is a muscular organ, pumping blood into the cardiovascular system through several billion cycles during a human lifetime [14]. It facilitates the essential processes of gas and nutrient exchange throughout the body, without which no life would exist. Functionally, the heart can be divided into a left and right side, working as two separate pumps in a highly coordinated fashion [19]. Although the gross anatomy have been found to be considerably different, the two sides share the same operational principles [6].

The left heart can be further divided into two chambers; the LV and LA (see Figure 3.1). Likewise, the right heart is divided into the right ventricle and atrium [20]. In order to ensure a unidirectional flow between the chambers, four valves connect the different chambers in the heart [21]. The *atrioventricular* valves separate the atria from the ventricles. The MV separates the LA and LV, whereas the tricuspid valve separates the right atrium and ventricle. The aortic valve and pulmonary valve prevent backflow from the greater arteries into the ventricles, typically referred to as the *semilunar* valves due to their half-moon shaped leaflets (or *cusps*) [5]. The aortic valve is located between the LV and the aortic outflow tract, whereas the pulmonary valve separates the right ventricle from the main pulmonary artery (or: *pulmonary trunk*).

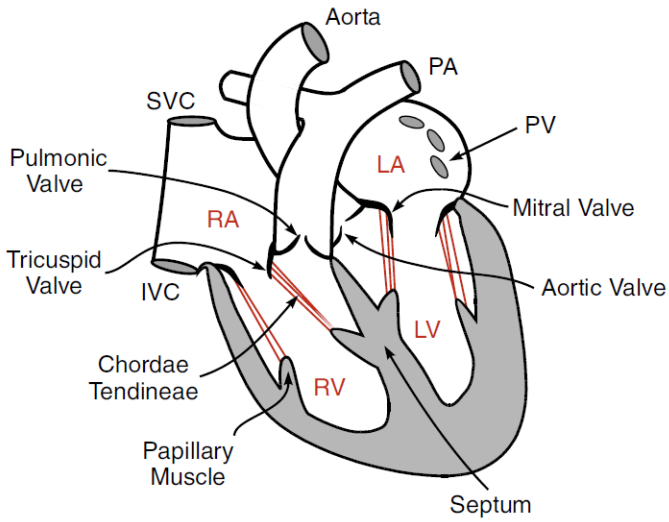

Figure 3.1: Cross-sectional view of the human heart. Adopted from [19].

The heart wall can be divided into three distinct layers: (1) the *endocardium*, (2) the *myocardium* and (3) the *epicardium*. The endocardium, the innermost layer, serves as an interface between the blood and chamber. It consists of single sheet of endothelial cells with a planar substructure of connective tissue. Thereafter follows the myocardium, which contains the muscular tissue of the heart wall. The tissue is composed of myocardiocytes, a muscle cell unique to the cardiac walls. These cells contract when subjected to electrical impulses, giving the heart its characteristic contractile behaviour. The myocardium is covered by the epicardium, a thin layer of connective tissue. Ultimately, the heart is enclosed by the pericardium, a fibrous sac suspending the heart through its attachment to the greater vessels. [6] Pericardial fluid lubricates the lining between the epicardium and pericardium, allowing the heart to function unconstrained [20].

The heart is the central pumping unit in the cardiovascular system. The cardiovascular system consists of the blood, the blood vessels, the heart as well as the lymphatic system facilitating the immune processes in the body [22]. The cardiovascular system can be further divided into two closed loop systems, namely the pulmonary and systemic circulations [19]. The right heart drives the blood through the pulmonary circulation, which is responsible for the gas exchange of oxygen and carbon dioxide in the lungs. The flow is initiated by the contraction of the right ventricle, ejecting the blood into the pulmonary trunk through the pulmonary valve. The pulmonary trunk divides into the left and right pulmonary arteries, leading to each lung, respectively. The arteries further branch significantly to a large grid of capillaries, blood vessels with a wall thickness of only a single cell. These vessels provide, in concert with the respiratory system, the necessary aids to promote gas exchange in the lungs [23].

The oxygen-enriched blood returns to the LA from the pulmonary veins, subsequently flowing into the LV through the MV. Thereafter, the blood enters the systemic circulation through the aortic valve following the contraction of the left ventricular walls. In the systemic circulation, the blood performs life-supporting

functions such as gas and nutrient exchange in the capillaries throughout the body.

Ultimately, the depressurized and deoxygenated blood returns to the right atrium from the superior and inferior vena cava. The cycle is completed as the blood flows into the right ventricle through the tricuspid valve, once again entering the pulmonary circulation. It should be noted that the left heart pressure is several times higher than the right heart pressure, indicating that the left heart is exposed to significantly higher loads, explaining why left heart diseases are overrepresented in a clinical setting (see Table 3.1). [24]

Table 3.1: Typical pressure ranges in the human heart. LV: Left ventricle, LA: Left atrium, RV: Right ventricle, RA: Right atrium. 1 mmHg = 133.322 Pa, values adapted from [19].

	LV	**LA**	**RV**	**RA**
p [mmHg]	10-120	8-10	4-25	0-4

3.2 The cardiac cycle

A sequence of highly coordinated events defines the distinct cyclic behaviour of the heart, typically referred to as the cardiac cycle [22]. The mechanical events that the heart undergoes during a cardiac cycle are tightly bound to the electrical activity in the heart, which relation can be instructively presented with a Wiggers' diagram (see Figure 3.2) [19]. The activity of the left heart is briefly described here, although the right heart share the same principles.

The sequence is initiated by the contraction of the atrial musculature (typically named atrial systole), following the electrical depolarization of the atria. In the electrocardiogram (ECG), this event is recognized as the p-wave. This is denoted as the very first wave in the ECG in Figure 3.2 [19]. The contraction further increases the atrioventricular pressure gradient, thus amplifying the blood flow into the LV. In fact, only about 10% of the total filling of the LV is accounted for by AC at normal heart rates, as the majority of the flow occurs before AC. However, the effect becomes increasingly more important at elevated heart rates as a result of vastly shortened filling periods, upwards of 40% of the total filling. [19, 21]

The LV then contract *isovolumetrically*, i.e without any change in volume. The contraction generates a rapid increase in left ventricular pressure (LVP), eventually equalizing the atrial pressure. Consequently, the MV closes whereas the LVP continues to rise (see Figure 3.2). Correspondingly, the characteristic QRS-complex can be observed in the ECG. The blood volume retained in the LV after closure of the MV is denoted the end diastolic volume (EDV). Simultaneously, the atrial pressure increases due to venous return of blood. [19]

The aortic valve opens as the LVP reaches the outflow tract pressures, rapidly ejecting blood into the aorta (see Figure 3.2). The atrial blood volume further increases,

although the atrial pressure initially decreases due to the atrial floor being pulled towards the LV by the atrioventricular pressure gradient. The LV is repolarized approximately 150-200 ms after the QRS-wave, relaxing the LV walls. The LVP decreases with the reduced blood volume, eventually falling below the outflow tract pressures. Consequently, the ejection rate is gradually reduced until the AV closes in order to prevent backflow into the LV (see Figure 3.2). [19]

Thereafter, a phase of isovolumetric ventricle relaxtion follows, where both valves are closed. The remaining blood in the LV after the systolic phase is denoted end-systolic volume (ESV). The stroke volume, the volume of blood pumped into the circulation during one cycle, is found as the difference between the ESV and EDV. The atrial pressure and blood volume further increase due to venous return of blood. [19]

The MV opens when the atrioventricular pressure gradient once again becomes negative (see Figure 3.2). The blood flows into the LV rapidly, as the atrial blood volume is maximal prior to opening. Additionally, a suction effect is generated as the myocardium recoils elastically from its systolic deformed state [25]. The flow is passive, as the atrial walls have not yet contracted. Eventually, the passive flow is gradually reduced as the atrioventricular pressure gradient declines, a phase known as diastasis [25]. Ultimately, the cycle is completed as the atrial walls once again contract.

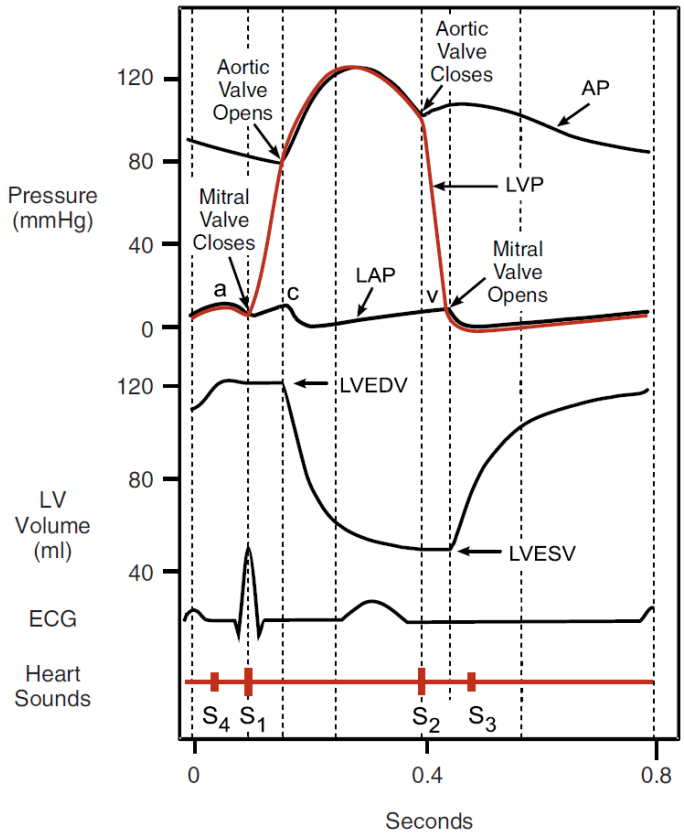

Figure 3.2: A Wiggers diagram showing the coordinated variation of cardiac quantities. The different quantities have been denoted on the left side of the figure. Adopted from [19].

3.3 The mitral valve apparatus

The MV ensures a unidirectional blood flow between the LA and LV, ideally maximizing the flow rate whilst minimizing flow resistance. The name originates from its strong resemblance to a bishop's mitre in its closed configuration, although its two leaflets explains why it is also referred to as the *biscupid* valve [5, 26]. The complete MV apparatus is comprised of various anatomical parts, more specifically the MV leaflets, the papillary muscles, chordea tendineae, the mitral annulus (MA) and the LA wall.

3.3.1 The mitral valve leaflets

The two leaflets, the anterior mitral leaflet (AML) and posterior mitral leaflet (PML) are found be be larger and stronger than those in the tricuspid valve, their right heart counterpart [5]. The AML is in fibrous continuity with the aortic valve, and covers about $^1/_3$ of the atrioventricular circumference. It has a rounded free edge, and is separated from the PML by an ill-defined closure line. [27] The junctioning regions where the leaflets abut are named the anterolateral commissure (ALC) and posteromedial commissure (PMC), respectively, marking each end of the closure line. The commissures end about 5 mm short of the MA in a healthy adult heart, therefore no distinct cut divisions exist between the two leaflets [26].

The PML is on a general basis divided into three segments (or *scallops*) along the free edge, denoted P1, P2 and P3 respectively (see Figure 3.3), although studies show that this number can vary slightly without necessarily implying pathological conditions [28]. The indentations are usually not in contact with the MA, a diseased state which is typically associated with MR [27]. The indentations have not been found along the anterior free edge, however the AML is for descriptive purposes divided into A1, A2 and A3 corresponding to the PML segments (see Figure 3.3).

The leaflets are generally divided into three sections: A basal, rough and clear zone. The basal zone is unique to the PML, and is characterized by basal cords extending from the LV wall attached to its ventricular side. No similar cordal arrangement can be found at the AML. The clear zone, found towards the central region of each leaflet, is as the name suggests devoid of all cordal attachments. Finally, the rough zone is located near the notably thicker free edge of the leaflets. Extensive cordal arrangements can be found on the ventricular side, giving rise to characteristic nodular peaks on the atrial side of the leaflets. The cordal density tapers towards the commisures. [26, 27, 29]

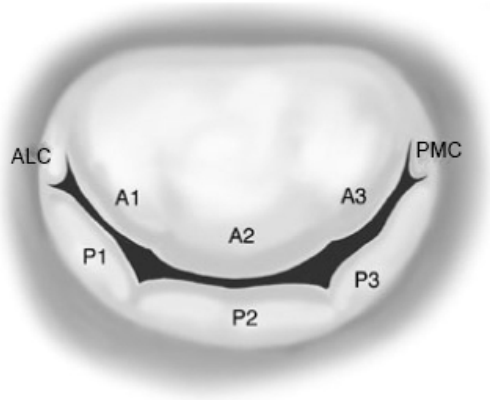

Figure 3.3: The mitral valve viewed from an atrial aspect. Adapted from [30].

3.3.2 Papillary muscles

The papillary muscles connects the tendinous cords to the LV walls [27]. Although it is often assumed that there are only two papillary muscles, it has been observed that there are often small groups of muscles arranged together. The muscle groups are typically referred to as the anterolateral (AL) and posteromedial (PM) papillary muscles, named after their location from an atrial aspect. [26]

In a normal functioning heart, the distance between the papillary muscle tips and the MA have been found to be nearly constant during systole. Moreover, abnormal papillary muscle motion is known to contribute to mitral insufficiency as the contraints on the MV leaflets are altered. In the event of a ruptured papillary muscle, the corresponding fibrous cords would be untensioned, resulting in incomplete coaptation of the MV leaflets. [31]

In vitro experimental studies found that the PM group was located closer to the apex in 67% of the examined hearts [32]. This has been independently verified by *ex vivo* clinical studies [33]. Furthermore, the total load was found evenly distributed between the two groups. The peak load occured in early systole, before gradually decreasing throughout the remaining systolic phase.

3.3.3 Chordae tendineae

The chordae tendineae is the fibrous cord network supporting the ventricular side of the leaflets. It is anchored in either the papillary muscles or directly to the LV wall. No cordal attachments have been found on the ventricular septum, in contrast to the tricuspid valve [34, 35]. The cords branch heavily from their anchoring point at the papillary muscles, attaching to both leaflets. On average 5 times as many cords attach to the leaflets as to the papillary muscles [36]. The delicate web formed constitutes a grid of pathways, allowing efficient blood flow into the LV. Histologically, the cords are composed of an inner layer of tighly bound collagen fibers giving them tensile strength (further elaborated in section 3.3.6). The outer layer consists

of more loosely bound collagen and elastic fibers, serving as a matrix for small blood vessel. It has been proposed that these vessels serve a nutritional role for the leaflets [37].

There are various classifications of the tendinous cords available, typically based on either their anatomical or physiological role. Traditionally, they have been grouped into first, second and third order cords, according to their leaflet insertion point. The first order cords insert on the leaflet free edge, and form as mentioned delicate webs near the edge [26]. Their main responsibility is to ensure complete coaption of the leaflets [35]. This is followed by the second order cords, which task is to maintain leaflet geometry throughout a cardiac cycle. They anchor in the rough zone, and have been found notably larger compared to the first order cords. Lastly, the third order cords are unique to the PML, and correspond to the aforementioned basal cords. Originating from the LV wall, they have been found to be essential for the ventricular geometry and reinforcing the annular region of the PML [35].

Subsequent studies have emphazised specific cords due to their important physiological roles, such as the commissural, strut and cleft cords [29]. The commissural cords support the free margins of the commissural regions, and there is normally only one cord supporting each commisure. Their presence ensure a correct coaptation during MV closure. Furthermore, two second order cords on the AML have been found distinguishly larger and thicker than the rest. They are called the strut cords, and are supposedly the largest and strongest of the cords [26, 29]. Lastly, the cleft cords have only been found on the PML, as they support the indented regions of the leaflet. Typically, two cleft cords divide the leaflet into the mentioned three scallops [29].

3.3.4 The mitral annulus

The MA is defined as the hingeline between the leaflets and atrioventricular orifice. It is D-shaped viewed from a plan view, allowing the aortic valve to be wedged in between the ventricular septum and MV [5]. The fibrous continuity with the aortic valve extends along the MA towards the commissures as the left and right fibrous trigone, respectively. Although fibrous prongs of tissue have been traced from the trigones, these have not been continuous around the orifice, where studies have demonstrated distinct variations in even the same heart [27, 38]. The posterior part of the MA is therefore more prone to dilatation than its anterior counterpart [26]. Experimental studies have validated that the anterior part is virtually unaffected to perimeter change, whereas the posterior side have shown a contraction upwards of 10% during systole [12].

The peaks of the saddle shape are found anteriorily and posteriorily, whereas the valleys are located medially and laterally. The height of the saddle peak is named the saddle height, which is found to increase slightly during systole [39]. The in-plane distance between the ALC and PMC is denoted the commissure width (CW), whereas the in-plane distance between the anterior and posterior peaks is called the septal-lateral length (SL). The former is typically larger, giving rise to the slightly

elliptical planar view [40]. The measures have been found to change significantly during a cardiac cycle, varying between maxima in diastole and minima in systole. The distances reduce asymmetrical during systole, further increasing the deviation from a circular shape [41].

The MA area has been found to be largest at end diastole and smallest during systole [42]. Accompanied by an increased saddle height and reduced SL distance, the nonplanarity of the MA increases during systole [39].

3.3.5 The left atrial wall

Due to its continuity with the MV leaflets, the LA wall has been appreciated as an important part of the MV apparatus [26]. It was postulated as early as in 1843 that AC was a crucial element for the presystolic closure of the MV leaflets [15]. Importantly, it became evident that the closure of the MV leaflets is governed by a complex series of both atrial and ventricular events.

More recently, two main contributions of the LA have been highlighted: (1) contraction and relaxation and (2) dilated atrial walls [43].

It has been proposed that contractility of the LA rather than blood flow is the main contributor to closure of the MV leaflets, although there is an ongoing controversy regarding their relative contribution [16]. Notably, the contraction of the LA have been held responsible for generating a reverse pressure gradient between the LA and LV *before* the onset of ventricular systole [43].

A dilated atrial wall directly affects the posterior MA, absent of the aforementioned fibrous continuity seen on the anterior side. Following dilation, the posterior wall undergoes posterior and downwards displacements, eventually tensioning the PML due to endocardiac continuity. Ultimately, this might hinder a full closure of the MV leaflets [43]. In a recent study, it was concluded that not only the dilated MA, but in fact also the atriogenic tethering of the PML could reduce the coaptation of the MV leaflets [18].

Atrial fibrillation (AF) is a disease which heavily affects the contractile behaviour of the atrial walls [17]. A recent study indicated that isolated LA enlargement and a dilated MA in AF patients was a prerequisite but not a *sufficient* condition to cause MR without coexisting abnormal LV systolic deformation [44].

3.3.6 Leaflet mechanobiology

From a cross-sectional view, the MV leaflets are found to have a distinct layer-wise composite structure, analogous to structure seen in the aortic valve [14, 45]. The main constituents of the valve tissue are the extracellular matrix (ECM), various proteins as well as the valve interstitial cells (VICs). These cells are specialized in the replenishing and remodelling of the ECM. The four layers, the atrials, spongiosa,

fibrosa and ventricularis, each have their distinctive thickness, cell environment and structural composition that contributes to the global functioning valve.

Mechanics of the mitral valve leaflets

The mechanical properties of the MV leaflets are mainly given by the interplay between collagen and elastic fibers. Collagen is a fibrous protein constituting about 30% of the total body protein, providing a structural framework and mechanical strength to nearly all tissues in the human body [46, 47]. The collagen fibers are composed of large bundles of fibrils, inheriting from the precursor tropocollagen [48]. Collagen fibers have been widely studied, where recent experimental studies have found the Young's modulus to be 1.2 GPa [46, 49, 50]. Furthermore, the ultimate tensile strength $\sigma_{\mathbf{UTS}}$ and failure strain $\epsilon_{\mathbf{max}}$ have been found as 120 MPa and 13%, respectively (see Table 3.2) [51].

Elastin, a highly elastic protein, constitutes more than 90% of the elastic fibers [46]. Structurally, it is composed of a large network of cross-linked tropoelastin, a highly elastic molecule [52]. The elastic properties of elastin has been devoted to entropic deformation, i.e. uncoiling and ordering of the network in space. Elastin exhibits rubber-like mechanical properties, offering low stiffness and very large extensibility compared to collagen fibers. The Young's modulus is approximately 1000 times smaller than that of collagen, whereas the failure strain $\epsilon_{\mathbf{max}}$ reaches values of more than 150% (see Table 3.2) [46, 47].

In fact, elastin is a viscoelastic material, showing strong dependencies on loading rate and environmental effects. However, under the conditions seen in the human body, elastin can be reduced to one of the most linear biosolids known [53]. In order to work efficiently during a cardiac cycle, the loading and unloading curve should ideally coincide, implying no loss of elastic energy [54]. Although both elastin and collagen show some hysteresis behaviour, the elastic energy loss during a loading cycle has been found to be less that 10% under physiological loading conditions [46]. In fact, elastin is *not* remodelled during the lifespan of an animal, setting strict requirements on the fatigue behaviour. Fatigue tests have in fact revealed that the fatigue life of elastin is similiar to a human lifetime under physiological loading [53]. Genetic disorders leading to fragmentation of elastic fibers have therefore shown to have very high mortality rates [50].

Table 3.2: Relevant mechanical properties of elastin and collagen fibers.

	Young's modulus [MPa]	$\sigma_{\mathbf{UTS}}$ **[MPa]**	$\epsilon_{\mathbf{max}}$ **[-]**
Elastin [46, 50]	1.1	2	1.5
Collagen fibers [46, 53]	1200	120	0.13

Ultimately, the MV leaflets have been characterized as an anisotropic, quasi-elastic material [55]. The anisotropy is derived from the heterogenous distribution of components throughout the leaflets, leading to highly directional-dependent properties.

The mechanical response resembles, as virtually any other collagenous tissue, a J-shaped curve (see Figure 3.4) [47, 50, 53]. Due to chemical interaction with the ECM, the collagen fibers show a large degree of crimp in their unloaded, *in vivo* configuration. This explains the initial toe region of the response curve seen in Figure 3.4, where the collagen fibers neither have been recruited nor uncoiled. The majority of the load is therefore carried by the elastic fibers, providing much lower stiffness. As the collagen fibers are gradually recruited, the stiffness increases correspondingly. Ultimately, the load is carried fully by the collagen fibers, lead to a drastically increased stiffness (see Figure 3.4b).

The quasi-elastic description inherits from extensive bi-axial testing regimes, showing a virtual independence on cyclic loading rate in the physiological range [55]. Furthermore, the stress relaxation was large, in contrast to no observable creep. The global hysteresis was found to be around 12%, in line with the results presented for each constituent. As with any other biological tissue, the MV leaflets are prone to preconditioning effects under altered loading conditions [47]. The effect is manifested through an enlarged hysteresis loop, that decreases with time as the structural composition is stabilized [50].

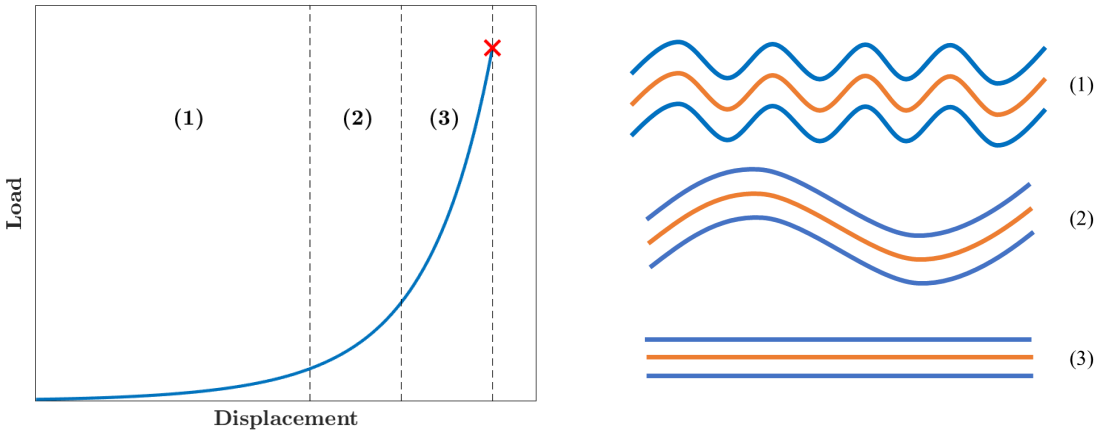

(a) Response curve **(b)** Reduction of crimp

Figure 3.4: A typical response curve of a collagenous tissue. The curve can be divided into three distinct sections: (1) The load is largely carried by elastic fibers with very low stiffness. The collagen fibers exhibit large crimp in this region. (2) The collagen fibers are gradually recruited and oriented, carrying an increasing part of the load. (3) The collagen fibers are fully recruited, carrying the vast majority of the load. The stiffness of the tissue increases correspondingly. The material fails at the failure strain, shown with a red cross in Figure 3.4a. Figure inspired by [50].

Mitral valve leaflet composition

The atrialis faces as the name suggests the atrial side of the MV apparatus (see Figure 3.5). Its surface is covered with a layer of endothelial cells (endothelium). Normal functioning endothelial cells is critical for maintaining healing and regulatory functions in the valve, in order to maintain valve *homeostasis*. [56] A layer of radially aligned connective tissue is found beneath the endothelium, originating from the left atrial endocardium. This layer, with its interspersed elastin sheets and collagen

fibers, enables the valve to elastically recoil during diastole, avoiding dynamic tissue creep [14]. As the MV undergoes several billions of cycles, this function becomes a critical attribute over time.

The spongiosa is located adjacent to atrialis (see Figure 3.5). It is characterized by a high concentration of proteoglycans and glycosaminoglycans, two highly hydrophilic molecules that are contained in the ECM. The presence of these molecules leads to a water retainment in the leaflets, imparting a vastly increased viscosity. The compressibility of the leaflets are therefore drastically reduced, explaining why they are typically assumed to be incompressible [55].

The fibrosa is in fibrous continuity with the MA, and consists mainly of a planar arrangement of collagen fibers (see Figure 3.5) [14]. The fibers are circumferentially aligned, providing the necessary mechanical strength to withstand the physiological loading. The majority of the load is carried by the fibrosa, in addition to providing the necessary mechanical integrity to the MV leaflets [50].

The ventricularis share the same composition and role as the atrialis (see Figure 3.5). As the interspersed collagen fibers in these layers are randomly oriented, they have been found to be much more flexible compared to the fibrosa [50].

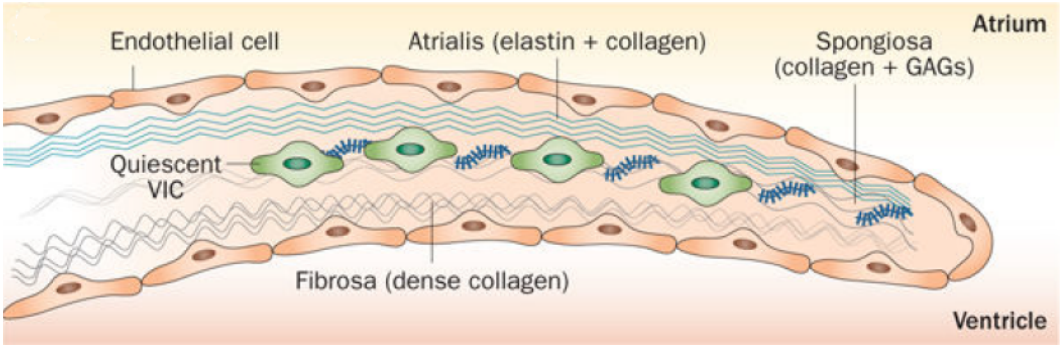

Figure 3.5: Physiology of the MV leaflets. The four different layers of the leaflet have been indicated in the figure. Adapted from [14].

3.4 Continuum mechanics

A continuum body is considered, assumed to be undeformed in its reference configuration Ω_0. $\mathbf{X}$ describes the position of an arbitrarily particle in Ω_0, whereas the mapping of each particle to the current configuration Ω is given by $\mathbf{x}(\mathbf{X}, t)$ [54]. From this, the *deformation gradient* $\mathbf{F}$ can be defined as:

$$\mathbf{F} = \frac{\partial \mathbf{x}}{\partial \mathbf{X}} \tag{3.1}$$

which per defintion describes the mapping of infinitesimal line elements between the two configurations:

$$d\mathbf{x} = \mathbf{F} d\mathbf{X} \tag{3.2}$$

The *volume ratio* is defined as $J = \det \mathbf{F} > 0$, where $J = 1$ for an incompressible material. Thereafter, the right and left Cauchy-Green tensors are defined as $\mathbf{C} = \mathbf{F^T F}$ and $\mathbf{B} = \mathbf{F F^T}$, respectively.

In particular cases, it can be helpful to perform a multiplicative decomposition of $\mathbf{F}$ into a volume changing (dilational) and volume-preserving (distortional) part, given by (3.3) respectively [54]:

$$\mathbf{F} = (J^{1/3}\mathbf{I})\bar{\mathbf{F}} \tag{3.3}$$

The distortional part of the right and left Cauchy-Green tensors then follow as $\bar{\mathbf{C}} = J^{-\frac{2}{3}}\mathbf{F^T F}$ and $\bar{\mathbf{B}} = J^{-\frac{2}{3}}\mathbf{F F^T}$ respectively.

In a state of plane stress, the deformation gradient simplifies to:

$$[\mathbf{F}] = \begin{bmatrix} F_{11} & F_{12} & 0 \\ F_{21} & F_{22} & 0 \\ 0 & 0 & F_{33} \end{bmatrix} \tag{3.4}$$

In this case, the terms C_{i3} and B_{i3} for $i \neq 3$ in the right and left Cauchy-Green matrices reduces to zero. By applying the incompressibility condition, $J = \det \mathbf{F} = \sqrt{\det \mathbf{C}} = 1$, the term C_{33} can be derived as:

$$C_{33} = (C_{11}C_{22} - C_{12}^2)^{-1} \tag{3.5}$$

A *hyperelastic* material is a material that on an energetic basis can be described in terms of a scalar potential Ψ, here defined per reference unit volume. If the potential is solely a function of the deformation gradient $\mathbf{F}$, the potential is typically referred to as a strain energy function, from which the material stresses can be derived [54].

In terms of the MV apparatus, the anisotropic distribution of collagen fibers has to be incorporated. In fact, it has been found that strain energy function to a fiber-reinforced material with one family of fibers and transversely isotropic material symmetry depends only upon the right Cauchy-Green tensor $\mathbf{C}$ and the referential orientation of fibers, given by $\mathbf{a_0}$ [57]:

$$\Psi = \Psi(\mathbf{C}, \mathbf{a_0}) \tag{3.6}$$

This theory was further expanded in the works of Spencer in 1972, where it was shown that the same material could be described in terms of the five first tensor invariants [58]:

$$\tilde{\Psi} = \tilde{\Psi}(I_1, I_2, J, I_4, I_5) \tag{3.7}$$

Where I_1. I_2 and J are the principle invariants of $\mathbf{C}$ related to isotropic elasticity:

$$I_1 = \mathrm{tr}(\mathbf{C}), \quad I_2 = \frac{1}{2}[\mathrm{tr}(\mathbf{C})^2 - \mathrm{tr}(\mathbf{C}^2)], \quad J = \sqrt{\det(\mathbf{C})} \tag{3.8}$$

The transversely isotropic properties of the material is incorporated by the two last invariants I_4 and I_5, where I_4 describes the squared stretch in fiber direction in contrast to I_5 which is related to fiber shear deformation [59]:

$$I_4 = \mathbf{a}_0 \cdot \mathbf{C}\mathbf{a}_0, \quad I_5 = \mathbf{a}_0 \cdot \mathbf{C}^2\mathbf{a}_0 \tag{3.9}$$

For an *incompressible* transversely isotropic materials the strain energy function is further modified:

$$\bar{\Psi} = \Psi(I_1, I_2, I_4 I_5) + p(J-1) \tag{3.10}$$

where p is a scalar Lagrange multiplier used to enforce the incompressibility. From Equation 3.10 the second Piola-Kirchhoff stress tensor $\mathbf{S}$ can be derived as followed:

$$\mathbf{S} = 2 \sum_{\substack{i=1 \\ i \neq 3}}^{5} \frac{\partial \Psi}{\partial I_i} \frac{\partial I_i}{\partial \mathbf{C}} + p\mathbf{C}^{-1} \tag{3.11}$$

from which it follows that the Cauchy stress tensor is $\boldsymbol{\sigma} = \mathbf{F}\mathbf{S}\mathbf{F}^T$, obtained by the push-forward operation of $\mathbf{S}$. It is then deduced that the stress components $S_{i3} = S_{3i} = 0$ for $i = 1, 2, 3$ in a state of plane stress. Enforcing $S_{33} = 0$, the Lagrange multiplier can be determined from Equation 3.10:

$$p = -2 \sum_{\substack{i=1 \\ i \neq 3}}^{5} \frac{\partial \Psi}{\partial I_i} \frac{\partial I_i}{\partial C_{33}} C_{33} \tag{3.12}$$

3.5 Constitutive models

3.5.1 Mitral valve leaflets

Following extensive biaxial mechanical testing regimes and continuum mechanical analysis, May-Newman and Yin were able to formulate a constitutive model for porcine MV leaflet. The model considers both mitral valve composition and collagen fiber orientation, and establishes a strain energy function with three material parameters based on the experimental data. It is an invariant-based formulation, depending on I_1 and I_4 [11]:

$$\Psi(I_1, I_4) = c_0[\mathrm{e}^{c_1(I_1-3)^2 + c_2(\sqrt{I_4}-1)^4} - 1] \tag{3.13}$$

where c_0, c_1 and c_2 are the three material parameters. The implementation of the material parameters is presented in section 4.2.1.

A similar function to Equation 3.13 is one of the two anisotropic constitutive models readily available in ABAQUS/Explicit, developed by Holzapfel, Gasser and Ogden. Although initially developed to model arterial walls with distributed collagen fibre orientation, the model have served as a basis in the modelling of a wide range of tissues [10, 60]. The model is based on the deviatoric invariants of the right Cauchy-Green deformation tensor:

$$\bar{\Psi} = C_{10}(\bar{I}_1 - 3) + \frac{k_1}{2k_2}(\mathrm{e}^{k_2\langle \bar{E} \rangle^2} - 1) + \frac{1}{D}(\frac{J^2-1}{2} - \ln J) \tag{3.14}$$

with

$$\bar{E} = \kappa(\bar{I}_1 - 3) + (1 - 3\kappa)(\bar{I}_4 - 1) \tag{3.15}$$

Where $\bar{I}_1 = \text{tr}(\bar{\mathbf{C}})$ and $\bar{I}_4 = \mathbf{a}_0 \cdot \bar{\mathbf{C}}\mathbf{a}_0$, whereas C_{10}, k_1, k_2 and κ are material parameters. The operator $\langle \cdot \rangle$ is known as the Macauley brackets, and is defined as $\langle x \rangle = \frac{1}{2}(|x| + x)$ [61]. Note that the last term in Equation 3.14 is related to the compressibility, and will not be used in this study.

3.5.2 Chordae tendinae

The biomechanical properties of porcine MV chordae tendineae was recently investigated experimentally by Pokutta-Paskaleva *et al.* [62]. In this study, the chordal mechanical response was averaged by insertion point and leaflet type, before they were fitted to the Ogden strain energy function using $N = 1$ in equation Equation 3.16 [54, 61]:

$$\bar{\Psi}(\lambda_1, \lambda_2, \lambda_3) = \sum_{p=1}^{N} \frac{2\mu_p}{\alpha_p^2}(\bar{\lambda}_1^{\alpha_p} + \bar{\lambda}_2^{\alpha_p} + \bar{\lambda}_3^{\alpha_p} - 3) + \sum_{p=1}^{N} \frac{1}{D_p}(J-1)^{2p} \tag{3.16}$$

$\bar{\lambda}_i$ denotes the deviatoric principle stretches ($\bar{\lambda}_i = J^{-\frac{1}{3}}\lambda_i$), whereas μ_p and α_p are material constants. These have been implemented in section 4.2.2. Note that the last term in Equation 3.16 is related to the compressibility, and will not be used in this study.

3.6 Leaflet material orientation

In a study performed by Cochran in 1991, the collagen fiber distrubution was investigated using small angle light scattering (SALS) and polarized light microscopy (PLM) [63]. His findings reported a parallel fiber orientation in the center portion of the AML, gradually rotating adjacent to the strut cordal insertion points before ultimately turning orthogonal to the MA near the commissures, inserting into the fibrous trigones.

As no strut cords insert to the PML, the fiber orientation gradually rotates from parallel in the central portion to orthogonal near the commissures. Figure 3.6 shows the resulting mean collagen fiber direction mapped to the MV leaflets.

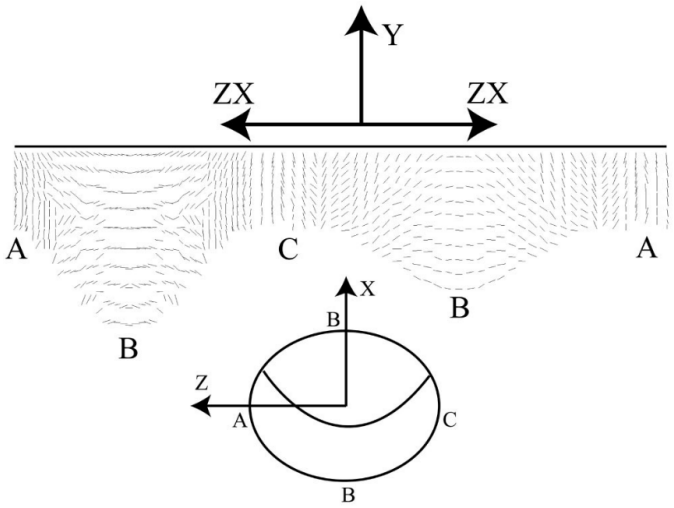

Figure 3.6: Collagen fiber orientation in the MV leaflets. SALS- and PLM-data generated by Cochran *et al.*, further investigated by Einstein *et al.* [63, 64].

3.7 Vectorial transformation laws

The vectorial transformation laws will later be needed to describe and rotate vectors in different coordinate systems. The theory is briefly presented here.

Two different coordinate systems are considered, with mutually orthogonal basis vectors (Figure 3.7). The systems share the same origin and are described by the two sets of basis vectors $\{\mathbf{e}_i\}$ and $\{\tilde{\mathbf{e}}_i\}$, respectively [54].

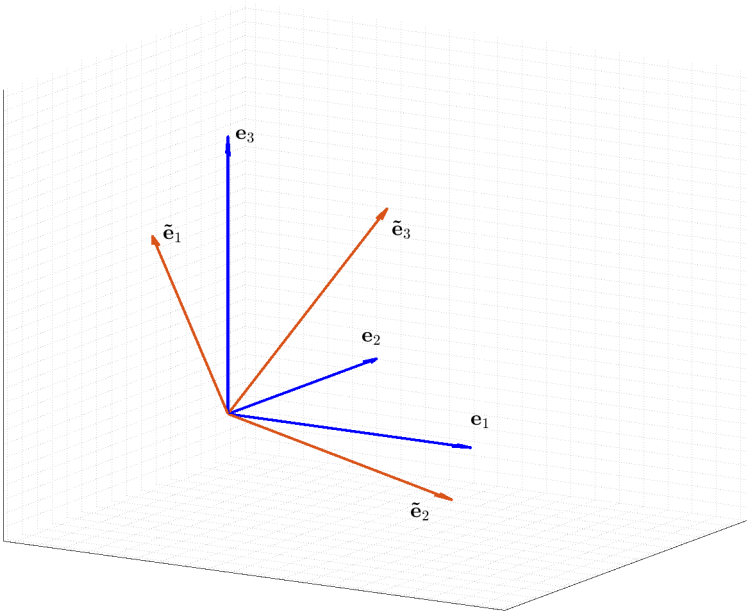

Figure 3.7: Two orthogonal sets of basis vectors. Generated using MATLAB [65].

The transformation law for change of basis is given by:

$$\tilde{\mathbf{e}}_i = \mathbf{Q}\mathbf{e}_i \ , \qquad i = 1,\, 2,\, 3 \tag{3.17}$$

where $\mathbf{Q}$ is a proper orthogonal tensor whose components are given by:

$$Q_{ij} = \mathbf{e}_i \cdot \tilde{\mathbf{e}}_j \tag{3.18}$$

The orthogonality and properness of $\mathbf{Q}$ implies that:

$$\mathbf{Q}^T\mathbf{Q} = \mathbf{Q}\mathbf{Q}^T = \mathbf{I} \qquad \text{and} \qquad \det\mathbf{Q} = 1 \tag{3.19}$$

which further renders $\mathbf{Q}$ orthonormal, preserving the length of the columns.

4. Methods

4.1 The Mitral Valve Model

4.1.1 Determining the reference configuration

In order to capture the effects of AC, the simulation was initiated before the onset of AC. Typically, the reference configuration of the MV is chosen at the instance of minimum LVP (LVP_{min}), ocurring in end diastole *after* AC (see Figure 3.2). In this configuration, the stresses in the MV are assumed to be at a global minima. However, in order to avoid the complexity of adding prestrains to the initial configuration, the reference configuration was simply shifted to before the onset of AC in mid diastole. This decision was based upon a study performed by Rausch *et al.*, who reported no significant difference between three diastolic reference configurations. [66]

4.1.2 Implementation of the load curve

The MV dynamics were simulated from mid diastole to end systole, capturing all the necessary parts of the cardiac cycle needed to investigate the effect of AC. The LVP curve was obtained using a micromanometer-tipped catheter (see Figure 4.1) [13]. The data was recorded over a time period of 0.420 s, discretized into 85 time increments. The LVP in the reference configuration was 5.0 mmHg, whereas the LVP in end systole was 33.2 mmHg. The maximum LVP applied was 74.2 mmHg, which occured at 0.255 s. No information about the atrioventricular pressure gradient or LA pressure was available. However, the atrioventricular pressure gradient is known to be very small relative to the LVP [19]. In this study, it was assumed to be *zero* in the reference configuration as no other information was available. Thus, the initial LVP was subtracted from the entire load curve. The load was applied as a uniform pressure load on the ventricular side of the MV leaflets in ABAQUS/Explicit [67].

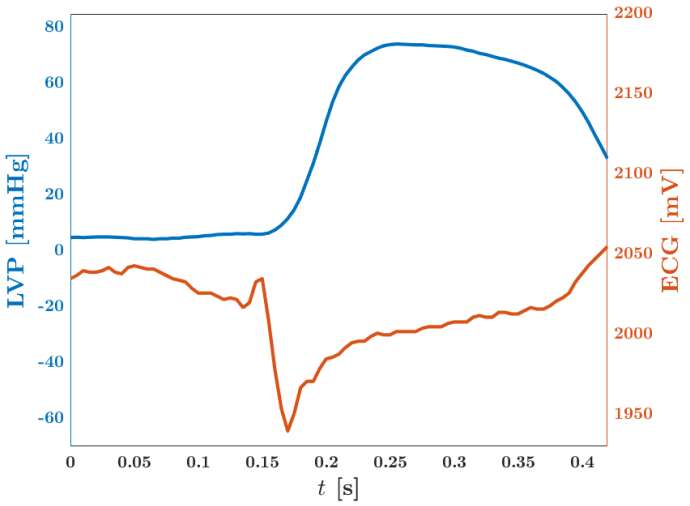

Figure 4.1: Pressure load curve generated from *in vivo* recordings. The blue curve shows the pressure load between mid-diastole and end-systole for a pig under normal physiological conditions. The ECG curve (orange) serves as a reference.

4.1.3 Extracting geometry from ultrasound recordings

US recordings was used to extract the geometry of the MV, which were processed using a graphical user interface (GUI) made in MATLAB [65]. The US recordings were organized in a three-dimensional coordinate system with one of the axes spanning the probe axis. The GUI enabled to either slice or rotate the pictures, allowing to manually select points at various orientations. This way, a point cloud of the tissue of the MV leaflets, the free edge line and the MA was extracted (see Figure 4.2).

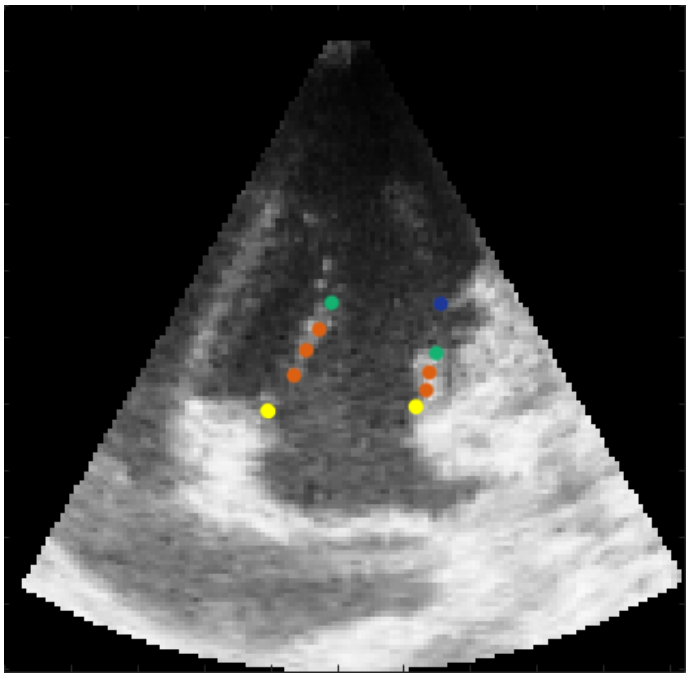

Figure 4.2: US image captured before the onset of AC. The MA (yellow), MV leaflet tissue (orange), MV leaflet free edge (green) and papillary muscles tip (blue) have been indicated in the figure.

4.1.4 Mitral annulus

To accurately track the deformation of the MA, crystals sutured onto the MA were used to track the deformation [13]. A total of eight crystals were used: One crystal was sutured in close proximity of each commissure, whereas three were equally spaced along each leaflet, respectively. Furthermore, three crystals were sutured to the outside of the heart, serving as fixed reference points. The MA geometry was then created using a built-in periodic cubic spline interpolating scheme in MATLAB with the crystal coordinates serving as interpolating nodes (see Figure 4.3). The crystal coordinates were recorded at a frame rate of 200 Hz, allowing the boundary to be tracked with high precision during a cardiac cycle.

In addition to the eight crystals located along the MA, one crystal was sutured to the apex (see Figure 4.3) [65]. As will be later discussed, this crystal allowed for verification of the US recordings, which data was obtained with the origin fixed at the apex (see section 5.1).

The interested reader is referred to the reference work of Dumont *et al.*, where a detailed explaination of the implementation of the crystals is provided [13].

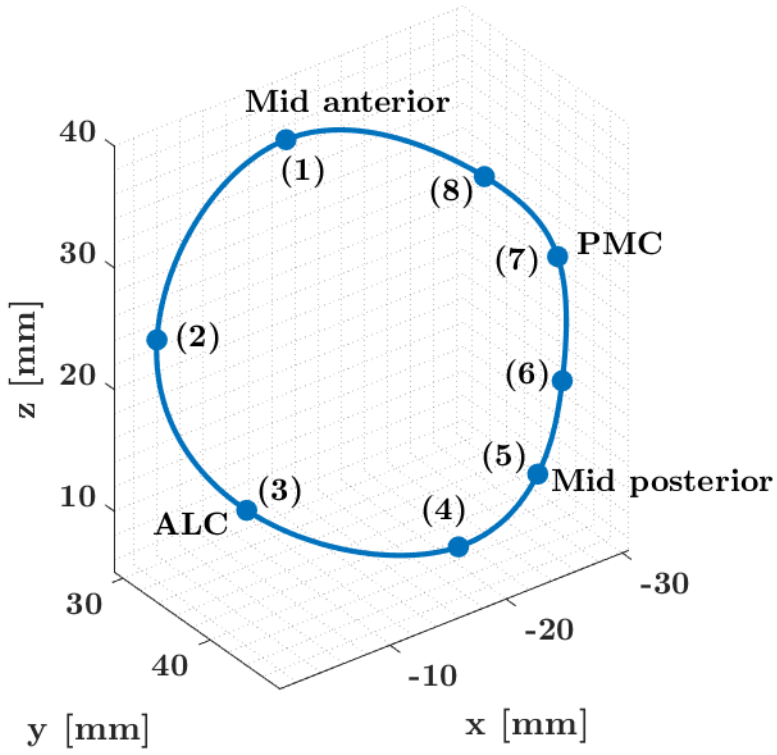

Figure 4.3: The position of the eight crystals along the MA in its reference configuration viewed from an atrial aspect. The position of the ALC and PMC have been indicated at the third and seventh crystal, respectively. Generated in MATLAB [65].

4.1.5 Coordinate transformation

As the crystal and US data were recorded in different local coordinate systems, a mapping of the US data into the crystal frame was necessary to assemble the model.

In order to map the data correctly, three corresponding orthogonal base vectors in each system were needed. They were created using the MA curve as a reference from both the crystal and US data. The procedure was initialized by generating a mean plane of the MA by using principal component analysis in the Optimization Toolbox in MATLAB [68].

Using the mean value of the MA as the local origin, the first base vector could then be identified as the in-plane projection of a known position vector. The anterior horn was chosen as a reference point, as it was possible to locate with relative ease in both data sets. Furthermore, the out-of-plane normal vector followed from the mean planes' orientation, whereas the second in-plane vector could be calculated using the cross-product of the two known vectors.

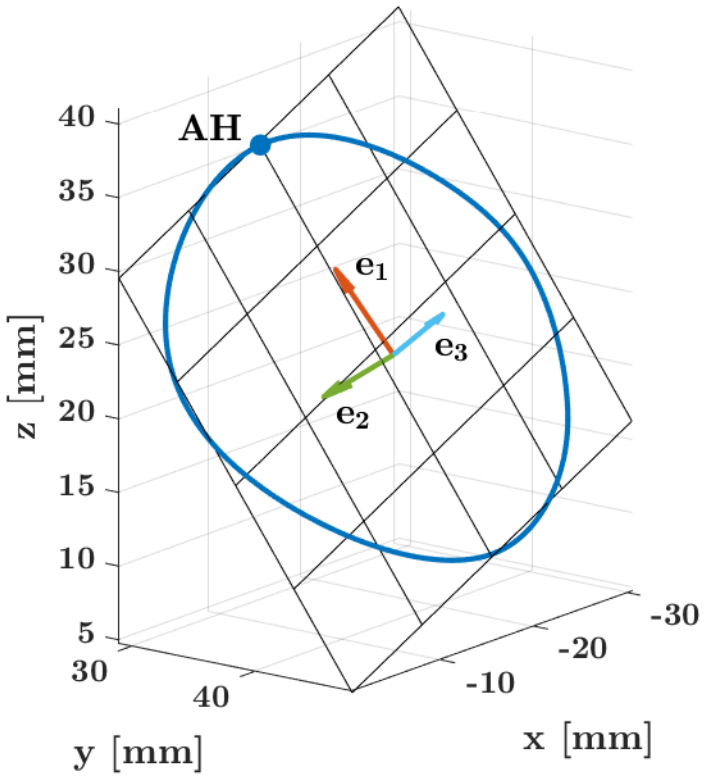

Figure 4.4: The reference configuration of the MA shown with an optimized plane of the geometry. The local coordinate system of the MA is shown. The anterior horn (AH) serves as the direction of the first base vector with origin at the mean of the MA. Note: The base vectors have been scaled with a factor of 7.5 for visualization purposes.

Using the vector bases, the current point vector $\mathbf{x}$ was rotated into $\bar{\mathbf{x}}$ according to Equation 4.1:

$$\bar{\mathbf{x}} = \mathbf{Q}^T\mathbf{x} \tag{4.1}$$

as presented in section 3.7. Ultimately, the rotated geometry underwent a rigid body translation into the crystal frame.

4.1.6 Assessment of the apex-relative motion of the mitral annulus

The relative motion of the MA with respect to the apex was needed to assess the relation between the US and crystal coordinate system (see Figure 4.5). Using the aforementioned optimized plane of the MA, the distance vector from the apex to the mean center of the MA ($\mathbf{d_{apex}}$) was projected into a normal and in-plane component, respectively.

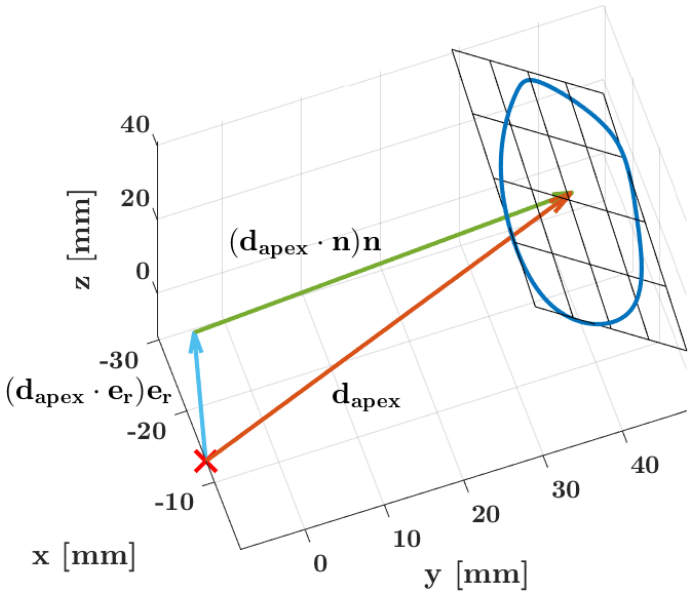

Figure 4.5: Clarification of the vector projections. The position of the apex have been shown with a red cross. The position vector from the apex to the mean center of the MA has been shown in orange. The radial and normal projections of this vector has been shown in light blue and green, respectively.

4.1.7 Annular dynamics

The MA dynamics were assessed using the CW, SL, the 3D perimeter and the annular area.

Calculation of the commisure width

The CW was defined as the length of the vector between the ALC-crystal (crystal no. 3) and PMC-crystal (crystal no. 7) in Figure 4.3.

Calculation of the septal- lateral length

Likewise, the SL was defined as the length of the vector between crystal no. 1 and crystal no. 5 in Figure 4.3

Calculation of the 3D perimeter

The 3D perimeter of the MA was defined as the length of the spline curve defined in MATLAB [65].

Annular area

The area of the MA was numerically calculated as the area confined by the optimized MA plane (see Figure 4.4) [65].

4.1.8 Generating a 3D model

In order to recreate the geometry of the MV the CAD software SOLIDWORKS was used [69]. The generated MA spline curve from the crystal data was imported together with the rotated and translated free edge and tissue points of the MV extracted from the US recordings. Thereafter, a free edge curve was generated as a spline in SOLIDWORKS (see Figure 4.6).

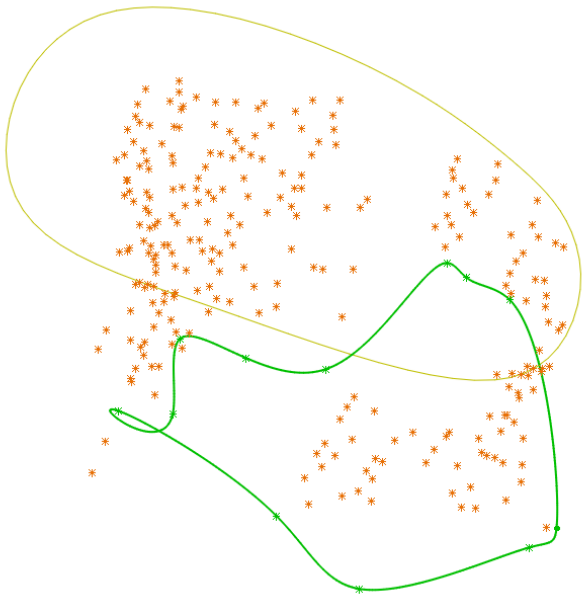

Figure 4.6: Point cloud of the MV leaflets. The MA (yellow line), MV free edge (green line) and MV tissue points (orange points) have been indicated in the figure.

An interpolated surface was then generated with the MA and free edge curves serving as the interpolating boundaries (see Figure 4.7).

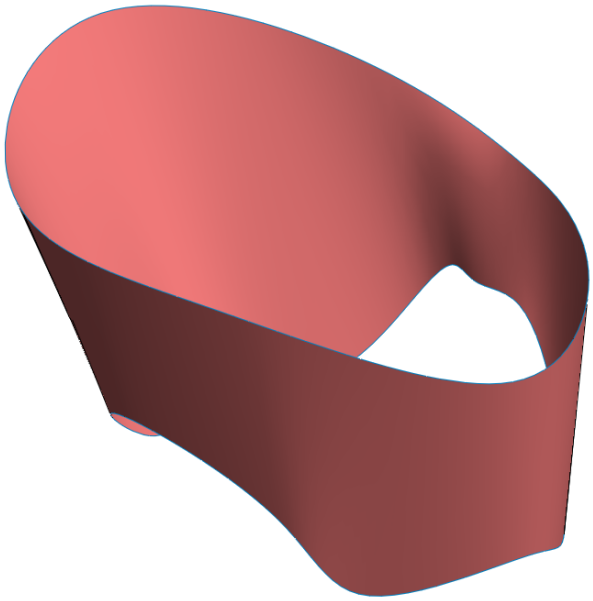

Figure 4.7: 3D surface of the MV leaflets in the reference configuration. Generated using SOLIDWORKS [69].

4.1.9 Papillary muscles

The position of the papillary muscles tips was extracted from US recordings as described in section 4.1.3. They were extracted from all relevant time frames, before they were identified with their corresponding crystal frames. Thereafter, their position was transformed into the crystal coordinate system by a coordinate transformation as described in section 4.1.5.

As the US recordings were obtained at a different frame rate than the crystal data, a fitting of the papillary muscle motion data along the time axis was needed (See Figure 4.8). 12 points were identified out of a total of 18 possible points in the relevant domain of the cardiac cycle. No US recordings were done during the QRS-complex.

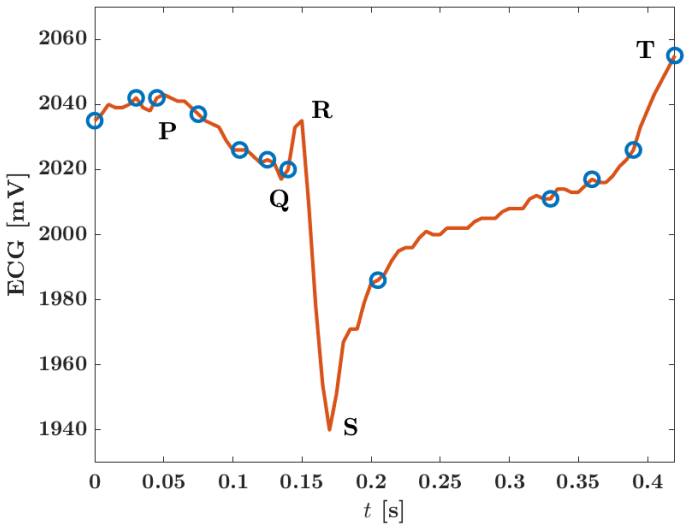

Figure 4.8: Fitting of papillary muscle motion data onto the time axis. The continuous line represents the crystal ECG, whereas the circles represents the discrete points that could be identified as corresponding events in the US ECG. The location of the distinct P-, Q-, R-, S- and T-wave have been indicated.

4.1.10 Prescription of boundary conditions

The MA and papillary muscle displacements, constituting the boundaries of the model, were both prescribed by utilizing the user subroutine VDISP for explicit analysis in ABAQUS [61]. The MA was prescribed at a rate of 200 Hz, whereas the papillary muscles, as further discussed in section 4.1.9, were only prescribed at certain landmark points of a cardiac cycle due to scarcity of the data (see Figure 4.8).

4.1.11 Chordae Tendineae

The chordae tendineae was anchored to the papillary muscle tips and inserted to their respective position on the MV leaflets. The basal cords were not modelled in this study, as their presence was taken into account by the prescribed MA BC. The marginal cords where inserted to both MV leaflets, whereas the strut cords were inserted to the AML rough zone exclusively.

The marginal chordae were initially distributed to simulate a anatomically correct model as described in section 3.3.3, but had to be adjusted to numerically stabilize the model.

The cross sectional area of the AML marginal and strut chordae was modelled to be 0.57 mm^2 and 2.50 mm^2 respectively. Furthermore, the PML marginal chordae was modelled using a cross sectional area of 0.40 mm^2 [62].

In ABAQUS/Explicit, the chordae tendineae was modelled using two-noded 3D truss elements (T3D2) [67]. The model generated in ABAQUS/Explicit can be seen in Figure 4.9 [67]:

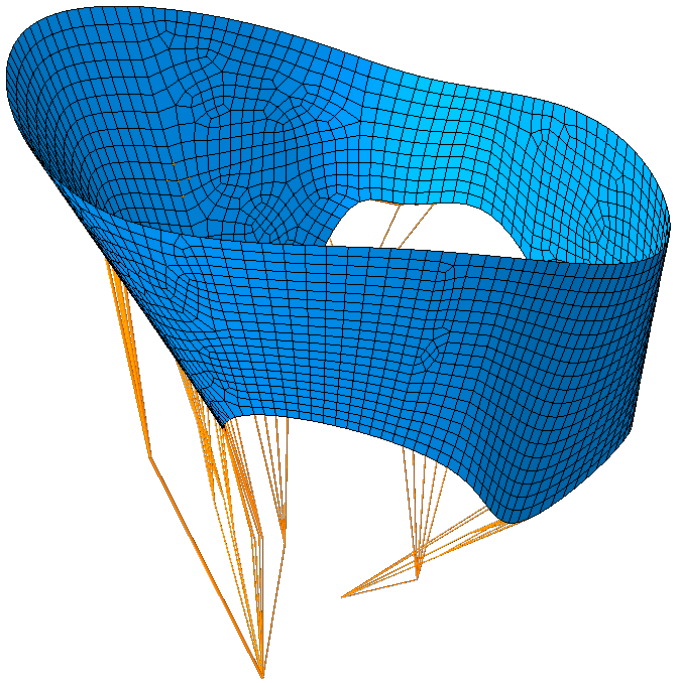

Figure 4.9: ABAQUS model of the MV apparatus. The MV leaflets are showns in blue, whereas the chordea tendineae are shown in orange.

4.1.12 Material orientation

In order to implement the fibre oriententation presented in section 3.6, the AML and PML where manually partitioned into several regions in ABAQUS/Explicit [67]. A local material orientation was then manually assigned to each region in order to match the fibre orientation previously presented in Figure 3.6. Figure 4.10 shows the obtained material orientation:

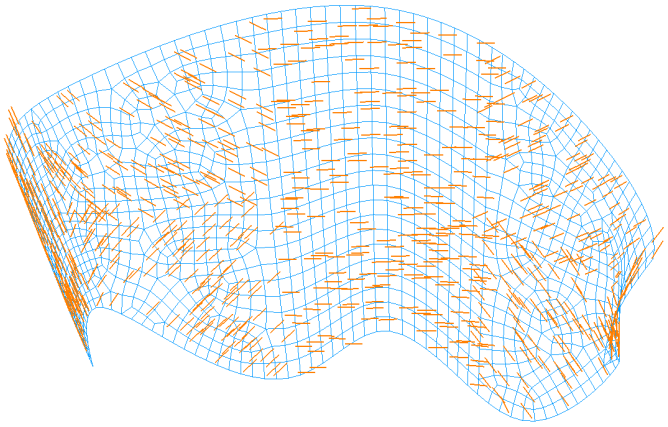

(a) AML

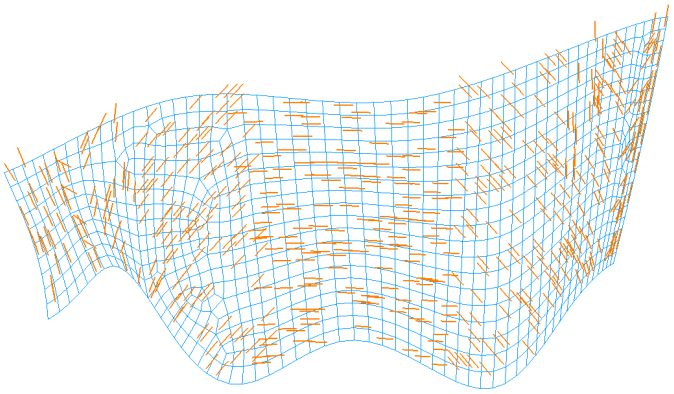

(b) PML

Figure 4.10: Local material orientation generated in ABAQUS/Explicit for the AML and PML [67].

4.1.13 Contact modelling

To model the contact mechanics of the MV leaflets a general contact algorithm in ABAQUS/Explicit was used. The normal contact direction was modelled as hard, whereas the tangential direction was assumed to be frictionless. [61]

4.1.14 Assigning thicknesses to the mitral valve leaflets

The AML and PML were modelled using constant thicknesses. The thicknesses were adapted from a previous study Pokutta-Paskaleva *et al.*, where average thicknesses of the MV leaflets were obtained. For the AML and PML, the thicknesses were modelled to be 1.14 mm and 1.30 mm, respectively [62].

4.2 Constitutive models

4.2.1 Mitral valve leaflets

Following the extensive biaxial testing regime performed by May-Newman and Yin, the following material parameters were obtained (see Equation 3.13):

Table 4.1: Material parameters obtained by May-Newman and Yin for the AML and PML [11].

	c_0 **[MPa]**	c_1 **[-]**	c_2 **[-]**
AML	0.399	4.325	1446.5
PML	0.414	4.848	305.4

The material model obtained by May-Newman and Yin was not available in ABAQUS/Explicit while this study was conducted. In order to avoid an implementation of the user subroutine VUMAT, the similar and readily available hyperelastic anisotropic material model in ABAQUS/Explicit developed by Holzapfel, Gasser and Ogden was used (see Equation 3.14). In a previous study, a nonlinear optimization study was performed to fit the response curve obtained by May-Newman and Yin to this model. The following material parameters were obtained [9]:

Table 4.2: Material parameters used for the Holzapfel, Gasser and Ogden-model, fitted from May-Newman and Yin [9].

	c_{10} **[MPa]**	k_1 **[MPa]**	k_2 **[-]**	κ **[-]**
AML	0.001	0.0240	50.92	0.1728
PML	0.001	0.0207	52.35	0.2669

4.2.2 Chordae tendineae

To model the response of the chordae tendineae, the Ogden constititive model was used as presented in section 3.5.2. The material parameter used in this study was adapted from a previous experimental study conducted by Pokutta-Paskaleva *et al.*. The following parameters were obtained after uniaxial testing of porcine MV chordae tendineae [62]:

Table 4.3: Material parameters used the Ogden constitutive model, adapted from a study conducted by Pokutta-Paskaleva *et al.* on the anterior strut, anterior marginal and posterior marginal chordae tendineae [62].

	μ_1 **[MPa]**	α_1 **[-]**
Anterior strut	1.31	65.27
Anterior marginal	2.27	32.42
Posterior marginal	20.23	49.34

4.3 Choice of element

4.3.1 Deformation characteristics of mitral valve leaflets

As explained in section 3.3.6, the MV leaflets are soft and pliable in their *in vivo* state [26]. Immediately, the bending stiffness is therefore expected to be much smaller than the in-plane membrane stresses.

Furthermore, as their planar extension is much larger than the thickness, the MV leaflets have typically been modelled as thin, planar structures. This implies that the stress space is reduced to a state of plane stress, as the out-of-plane stresses will be negligibly small.

Initially, the analysis was thought to be performed using membrane-type elements (M3D4), as they provide no bending stiffness other than that generated from geometrical contribution. However, since a stress free flat membrane has no stiffness perpendicular to the plane, out of plane loading will cause convergence difficulties and numerical instabilities due to a singular stiffness matrix [61]. Therefore, a large number of elements were prone to excessive distortion and warping, eventually leading to aborted simulations.

Therefore, the fully integrated finite membrane strain element S4 was used in this study. Since the stiffness of the element is fully integrated, no spurious membrane or bending zero energy modes exist [61]. S4 is based on thick shell theory, and is used in correspondence with a finite membrane strain formulation [70]. Therefore, this element is suitable for large strain analysis, also capable of preventing shear and membrane locking. It is a widely used element due to its capability of describing both thick and thin shells. [71]

4.3.2 Incompressibility of the S4 element

The incompressibility of the MV leaflets has to be numerically enforced in ABAQUS. This has proven difficult, as a Poisson's ratio close to 0.5 creates an ill-conditioned set of equations, possibly generating numerical instability and great loss of accuracy [72]. In ABAQUS/Standard, these issues can be avoided by using a hybrid element

formulation, where the nodal degrees of freedom only consider deviatoric stresses and strains. In ABAQUS/Explicit, no such method exists, other than increasing the ratio between the initial bulk modulus K_0 and initial viscosity μ_0 which increases the Poisson's ratio. However, the method should be applied with great caution, in order to avoid the above mentioned consequences. This problem is avoided in a plane stress configuration, where the thickness is allowed to deform freely, readily enforcing incompressibility.

Even though ABAQUS/Explicit states fully incompressibility for the S4 element, it was concerned that the incompressibility of the S4 element used in combination with the hyperelastic material model was incorrectly computed in ABAQUS/Explicit. Therefore, a test to verify the incompressibility was performed by modelling a pipe subjected to internal pressure. The radius of the pipe was 15 mm, close to that of the size of a MV leaflet [50]. Likewise, the pressure load applied had a maximum amplitude equal to the maximum pressure seen during a cardiac cycle (see Table 3.1).

Utilizing the axisymmetric properties of the geometry and loading, the system was modelled using a ¼ of the pipe cross section, with an initial pipe thickness of 1 mm (see Figure 4.11). The section was then assigned an S4 element type, with the hyperelastic model presented previously (see section 4.2.1). The assigned fiber orientation was in the *circumferential* direction. In order to achieve steady-state results, the load was applied as a smooth step with long step time, resembling a quasi-static load. The numerical approximation of the strucutral model generated in ABAQUS/Explicit has been shown in Figure 4.12 [67]. A summary of the values used have been presented in Table 4.4.

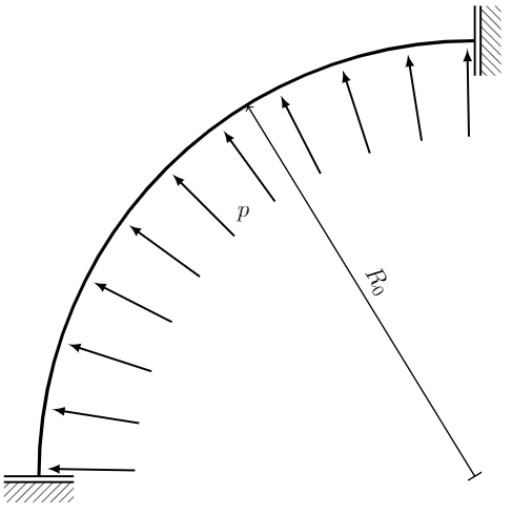

Figure 4.11: Structural model of a ¼ pipe cross section.

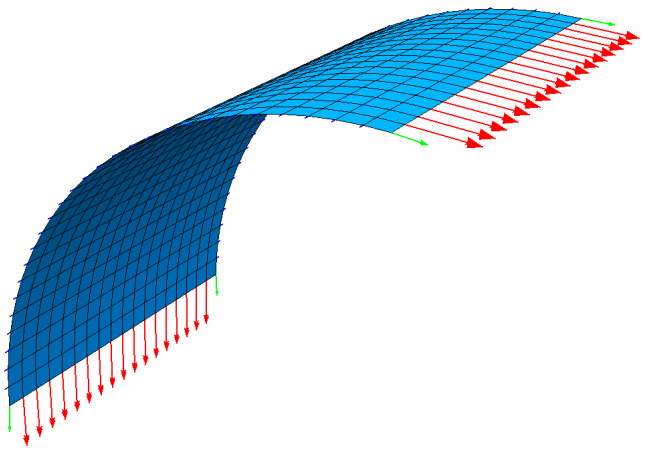

Figure 4.12: Numerical approximation of the structural model generated in ABAQUS/Explicit [67]. The corresponding reaction forces have been shown (red arrows).

Table 4.4: Initial values used during the element incompressibility test

	R_0 **[mm]**	p **[kPa]**	t_0 **[mm]**	w_0 **[mm]**
Value	15.0	15.00	1.0	15.0

Due to the axisymmetry, the deformation gradient takes the following diagonal form:

$$[\mathbf{F}] = \begin{bmatrix} \lambda_r & 0 & 0 \\ 0 & \lambda_\theta & 0 \\ 0 & 0 & \lambda_z \end{bmatrix} \tag{4.2}$$

where λ_r, λ_θ and λ_z represent the stretches in the radial, circumferential and longitudinal direction respectively. Defined as:

$$\lambda_r = \frac{t}{t_0}, \quad \lambda_\theta = \frac{R}{R_0} \quad \lambda_z = \frac{w}{w_0} \tag{4.3}$$

However, as the geometry is confined to displace in the $r-\theta$-plane, it is deduced that $\lambda_z = 1$. The relationship between the two remaining stretch components can then be found by enforcing the incompressibility condition:

$$\det \mathbf{F} = \lambda_r \lambda_\theta \lambda_z = 1 \Rightarrow \lambda_r = 1/\lambda_\theta \tag{4.4}$$

The following results were obtained from the analysis in ABAQUS/Explicit (see Table 4.5) [67]. The circumferential stretch λ_θ, radial stretch λ_r and the circumferential stress component σ_θ were obtained directly from ABAQUS/Explicit. The approximated circumferential stress component σ_θ^{app} was obtained as the current resultant force divided by the current cross sectional area. The normalized error ${}^{\Delta\sigma}/_{\sigma_\theta}$ was defined as:

$$\frac{\mid \sigma_\theta^{app} - \sigma_\theta \mid}{\sigma_\theta} \tag{4.5}$$

Table 4.5: An overview of the verification of incompressibility for different mesh densities.

Seed size [mm]	**# elements**	λ_θ [-]	λ_r [-]	σ_θ [**kPa**]	σ_θ^{app} [**kPa**]	$^{\Delta\sigma}/_{\sigma_\theta}$ [-]
6.00	12	1.2174	0.8214	327.06	333.47	$2.0{\cdot}10^{-2}$
3.00	40	1.2174	0.8212	332.05	333.65	$4.8{\cdot}10^{-3}$
1.50	160	1.2178	0.8212	333.30	333.70	$1.2{\cdot}10^{-3}$
1.25	228	1.2178	0.8212	333.42	333.70	$8.4{\cdot}10^{-4}$
1.00	360	1.2178	0.8212	333.53	333.71	$5.4{\cdot}10^{-4}$
0.75	620	1.2178	0.8212	333.60	333.71	$3.3{\cdot}10^{-4}$
0.60	975	1.2179	0.8211	333.64	333.71	$2.1{\cdot}10^{-4}$
0.50	1410	1.2179	0.8211	333.67	333.71	$1.2{\cdot}10^{-4}$

The analysis was performed on mesh densities ranging from element seeds between 6.00 mm (12 elements) and 0.50 mm (1410 elements). The incompressibility condition from equation (4.4) was satisfied for all the different mesh densities.

The normalized error decreased correspondingly with the reduced seed size. The normalized error was of order 10^{-2} when a seed size of 6.00 mm was used, reduced to the order of 10^{-4} as the seed size was reduced to 0.50 mm.

5. Results

5.1 Considering apex motion

As discussed in section 4.1.5, it became evident that the apex motion of either coordinate system had to be thoroughly investigated before a justified choice of dynamic frame could be made.

5.1.1 Crystal apex motion

The dynamics of the LV apex was analyzed using the position data extracted from the crystal recordings. The pathway of the apex was analyzed during a complete cardiac cycle (see Figure 5.1). A clearly cyclic motion can be observed through four distinct phases, representing (1) mid diastole, (2) late diastole/early systole, (3) mid systole and (4) late systole/early diastole. Furthermore, the absolute value of the instant velocity vector has been approximated using forward differences in time (Euler scheme) [72].

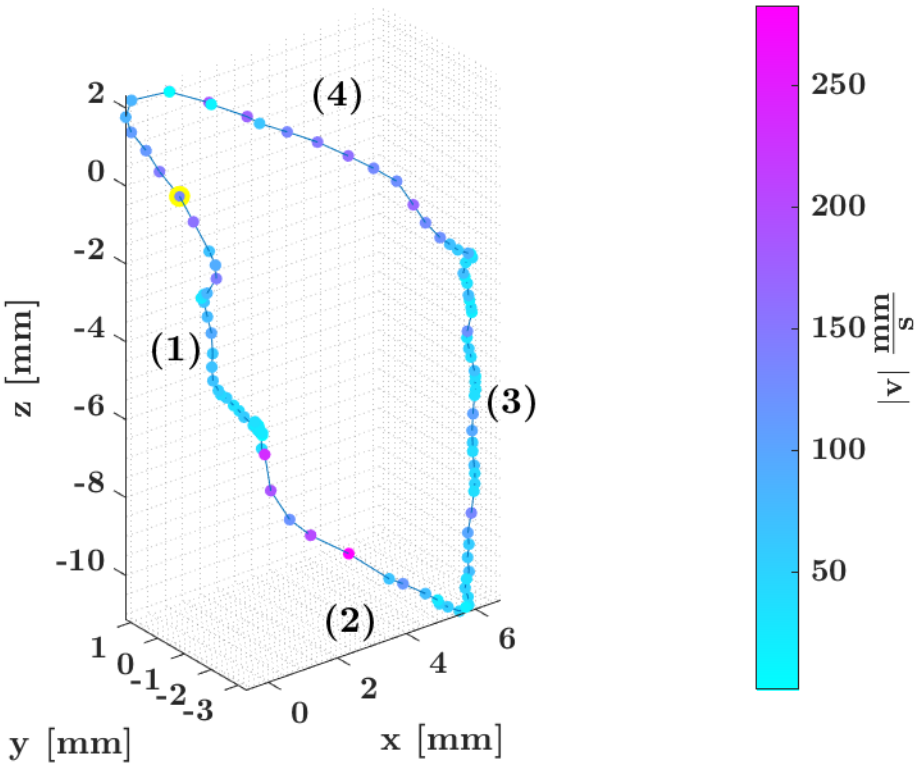

Figure 5.1: A 4-dimensional representation of the crystal apex motion with respect to the reference configuration (yellow ring). The pathway is represented as a thin blue line, whereas the velocity field has been approximated using forward differences. The colorbar represents the magnitude of the velocity vector, measured in $\frac{\text{mm}}{\text{s}}$. Four distinct phases can be readily observed: (1) Mid diastole, (2) late diastole/early systole, (3) mid systole and (4) late systole/early diastole. The difference between the maximal z-values were found to be 13.5 mm.

The apex crystal allowed the MA dynamics to be explored using both a fixed (static) and dynamic origin. As a first measure, the state space (complete set of points conformed) of the MA during a cardiac cycle was found using a static origin (see Figure 5.2). Four distinct configurations at landmark instances in the cardiac cycle indicated a downward-oriented motion of the MA.

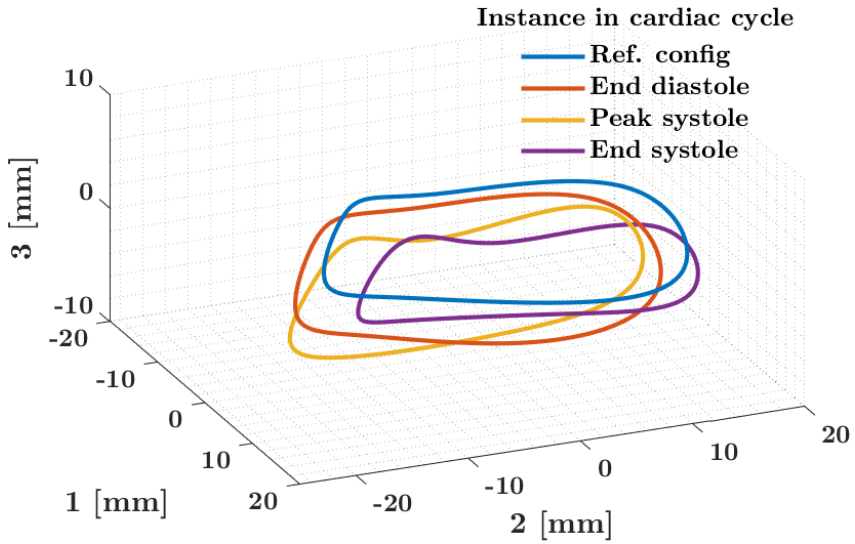

Figure 5.2: Four landmark configurations of the crystal MA using a fixed origin, shown with respect to the referential coordinate system of the MA (For an explaination of the local coordinate directions, see section 4.1.5).

Thereafter, the origin was translated to the apex. The state space was found in the same manner, indicating that the MA dynamics were altered significantly by the change of origin (see Figure 5.3). A clear sideways tendency with respect to the local 1-2-plane was be observed, differing from the 3-directed motion that the MA underwent with a static origin. Furthermore, a gradual rotation of the MA plane from the reference configuration into the peak systolic configuration could be observed.

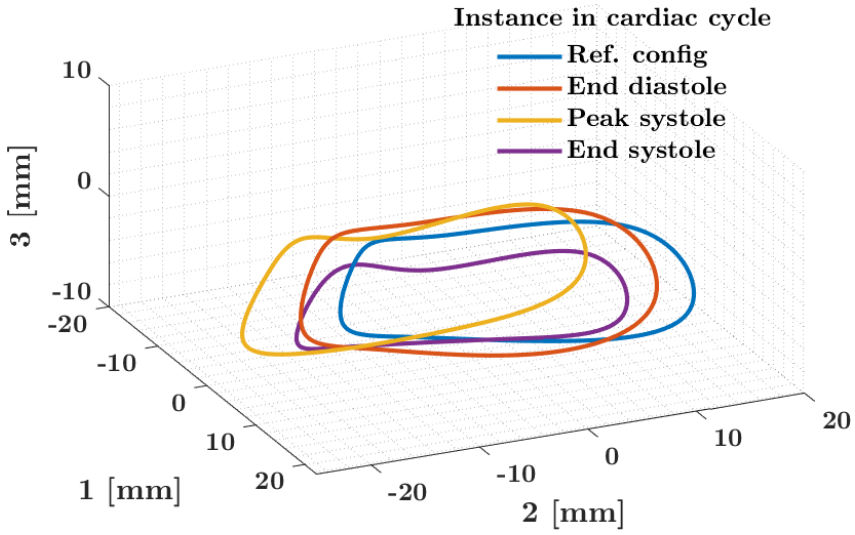

Figure 5.3: Four landmark configurations of the crystal MA corrected for a moving origin, shown with respect to the referential coordinate system of the MA (For an explaination of the local coordinate directions, see section 4.1.5).

In order to quantify the differences from the US recordings, the distance from the apex to the mean center of the MA along the current normal and in-plane direction

was investigated in the relevant sections of the cardiac cycle (see section 4.1.6). A distinct peak of 65.5 mm was found in early systole (near mid simulation time (0.220 s)) for the normal projection of the vector (see Figure 5.4). Thereafter, the distance steadily decreased towards a value of 56.2 mm near the T-wave. The distance was at a global minima of 56.0 mm in the reference configuration (mid diastole). The difference between the extremal values was 9.4 mm.

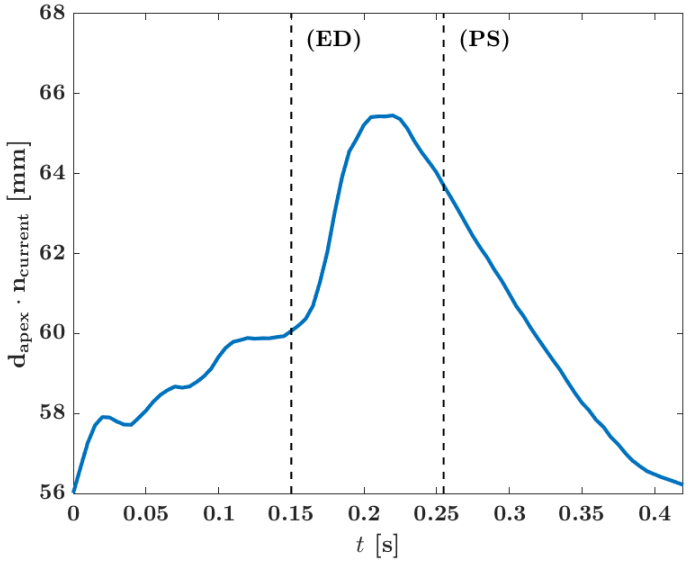

Figure 5.4: The distance from the apex to the mean center of the MA along the current normal direction to the MA plane. A distinct peak of 65.5 mm can be seen in early systole, before the distance steadily decreased towards the T-wave. The instances of end diastole (ED) and peak systole (PS) have been indicated in dotted vertical lines.

The component of the distance vector was then projected into the local $1-2$-plane, serving as a radial offset from the centerline of the MA (see Figure 5.5). The offset was 16.8 mm in the reference configuration. Thereafter, a local maxima of 18.3 mm was reached in late diastole, before the offset gradually increased to a global maxima of 20.1 mm.

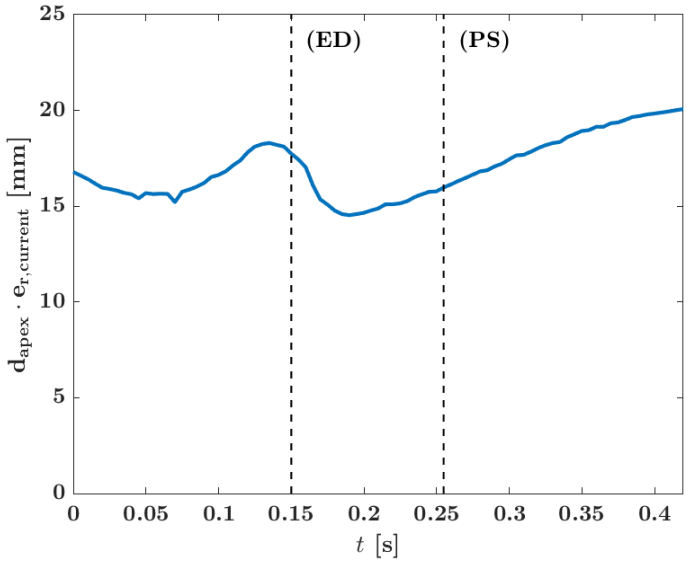

Figure 5.5: The radial offset of the apex from the MA centerline. A local maxima of 18.3 mm was observed in late diastole, before the offset steadily increased in the systolic phase. The instances of end diastole (ED) and peak systole (PS) have been indicated in dotted vertical lines.

5.1.2 Ultrasound apex motion

The same measures of apex motion were found from the corresponding MA generated from US recordings (see Figure 5.6). As the global coordinate system (which origin was located at at the probe end near the apex) underwent unknown rigid body motion, no mapping of the MA configurations to the referential frame could be performed (see Figure 5.6). In terms of motion, the US MA shared similarities with the crystal MA *without* correction for the apex motion. It was devoid of the sideways tendency observed in the corrected crystal MA. However, it should be noted that the motion was *oppositely* directed with respect to the reference configuration.

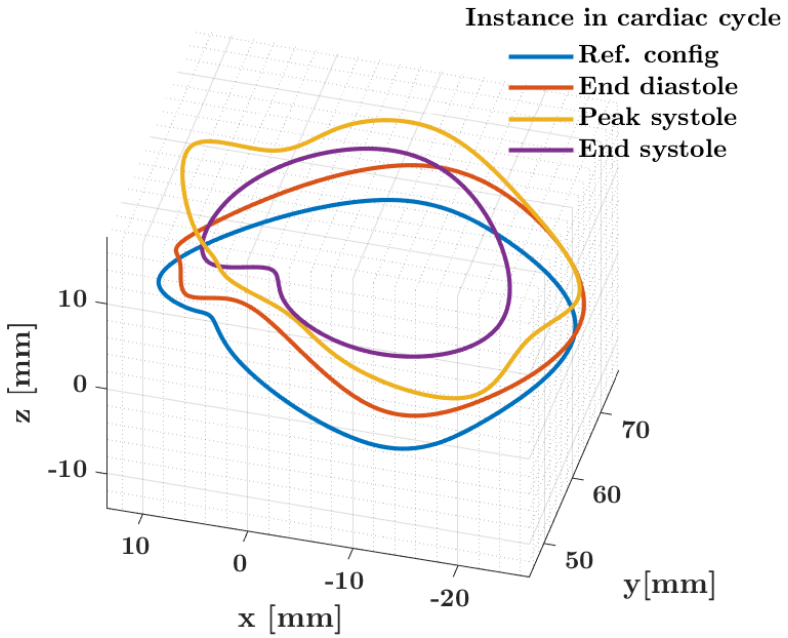

Figure 5.6: Four landmark configurations of the US MA recorded in a local coordinate frame. The origin was placed near the apex.

The position vector between the apex and MA obtained from the US recordings was projected in the same manner as the crystal data (see Figure 4.5). The distance along the normal direction was 58.0 mm in the reference configuration (see Figure 5.7). Thereafter, it followed a wave shaped curve through diastole, before abruptly reaching a global maxima of 67.6 mm in early systole. As mentioned in section 4.1.9, no data was recorded during the QRS-complex. Contrary to the normal projection of the crystal position vector, the normal projection of the US position vector remained close to its maximal value throughout systole. The distance in end systole was 65.5 mm. The difference between the extremal values was 11.0 mm.

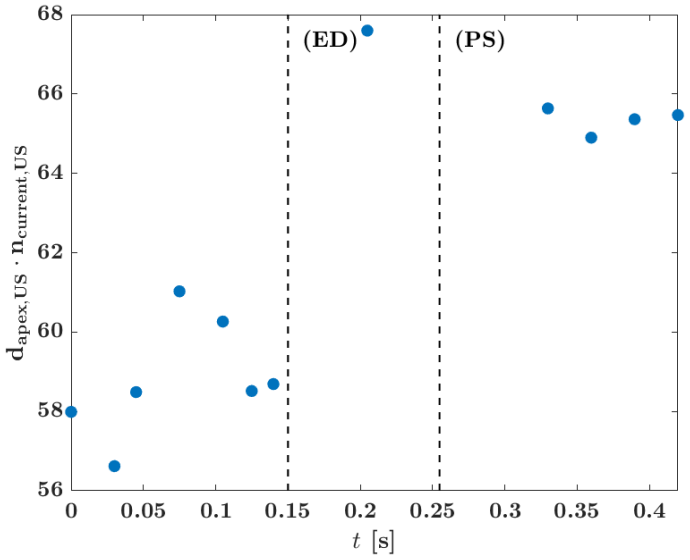

Figure 5.7: The distance from the apex to the mean center of the US MA along the current normal direction to the annulus plane. The 12 discrete recordings have been shown with blue dots. The instances of end diastole (ED) and peak systole (PS) have been indicated in dotted vertical lines.

The radial projection of position vector was 16.1 mm in the reference configuration (see Figure 5.8). Thereafter, it decreased during the diastolic phase before rapidly reaching a global maxima of 21.1 mm close to end diastole. The radial projection then decreased substantially after the QRS-complex, eventually reaching a global minima of 0.5 mm in end systole.

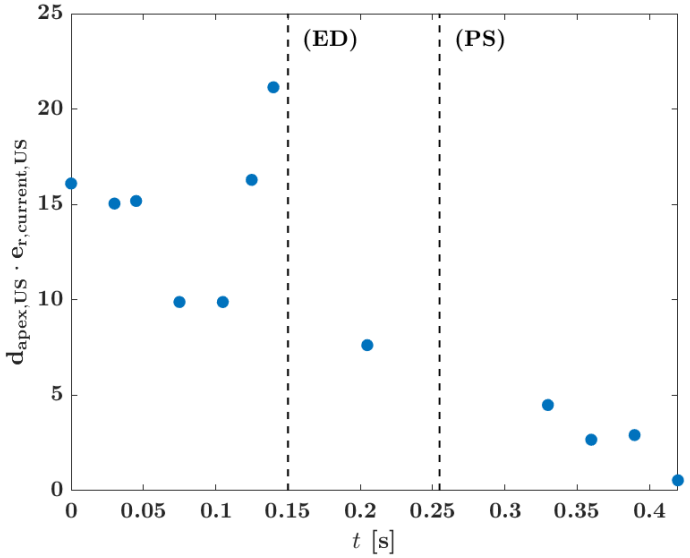

Figure 5.8: The radial offset of the apex from the centerline of the US MA. The 12 discrete recordings have been shown with blue dots. The instances of end diastole (ED) and peak systole (PS) have been indicated in dotted vertical lines.

5.2 Annular dynamics

The MA area, 3D perimeter, CW and SL were chosen as measures of MA dynamics (see section 4.1.7).

The MA area was nearly constant in mid diastole, before rapidly reaching a global maxima of 727.3 mm^2 during atrial systole (see Figure 5.9). Thereafter, it decreased towards ventricular contraction until reaching a local maxima towards the end of the QRS-wave. A decreasing trend was then seen through systole, before a global minima of 536.8 mm^2 was reached near end systole.

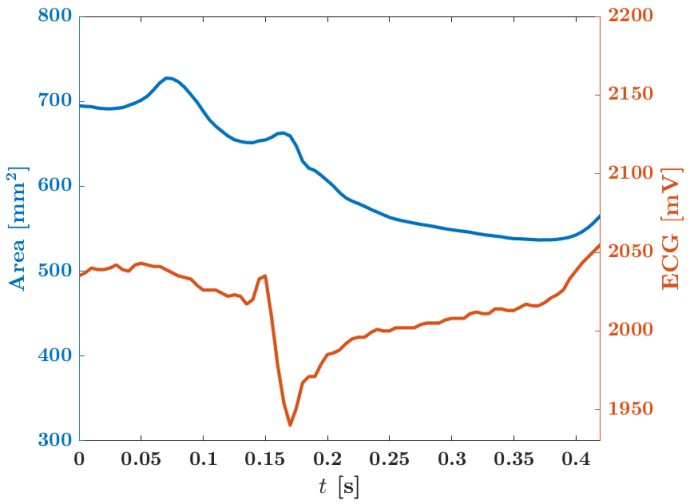

Figure 5.9: MA area recorded during the relevant sections of the cardiac cycle (see section 4.1.2). The area is shown with a blue line. The ECG curve (orange) serves as a reference

The perimeter reached a global maxima of 97.2 mm during atrial systole (see Figure 5.10). Thereafter, it decreased towards ventricular contraction, before a local maxima was reached towards the end of the QRS-wave. Thereafter, it decreased steadily during systole reaching a global minima of 84.2 mm. Ultimately, the perimeter increased towards end systole.

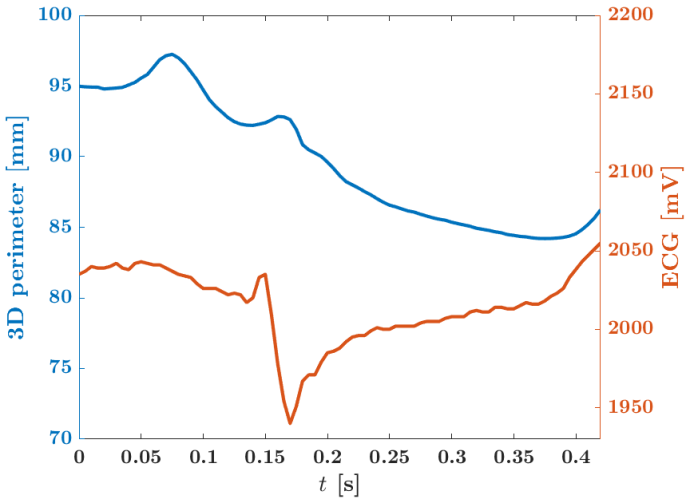

Figure 5.10: The 3D perimeter of the MA observed during the relevant sections of the cardiac cycle (see section 4.1.2). The perimeter is shown with a blue line. The ECG curve (orange) serves as a reference.

Initially, the CW was 29.7 mm (see Figure 5.11). Thereafter, it followed a wave-shaped path until early systole. The global maxima of 30.1 mm occurred during atrial systole, nearly identical to the local maxima in early systole. Thereafter, the CW decreased during the systolic phase, reaching an end value of 27.5 mm.

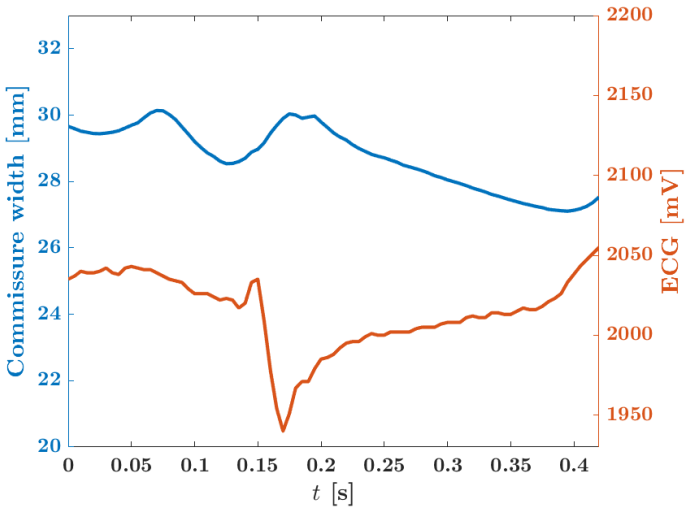

Figure 5.11: The CW observed in the relevant sections of the cardiac cycles (see section 4.1.2). The CW is shown with a blue line. The ECG curve (orange) serves as a reference.

The initial SL was 25.7 mm (see Figure 5.12). A subtle increase could be observed during atrial systole, where the global maxima of 26.1 mm was reached. Thereafter, the SL fell abruptly in early systole, eventually reaching a global minima of 22.6 mm near peak systole. Ultimately, the SL steadily increased in end systole, reaching an end value of 23.7 mm.

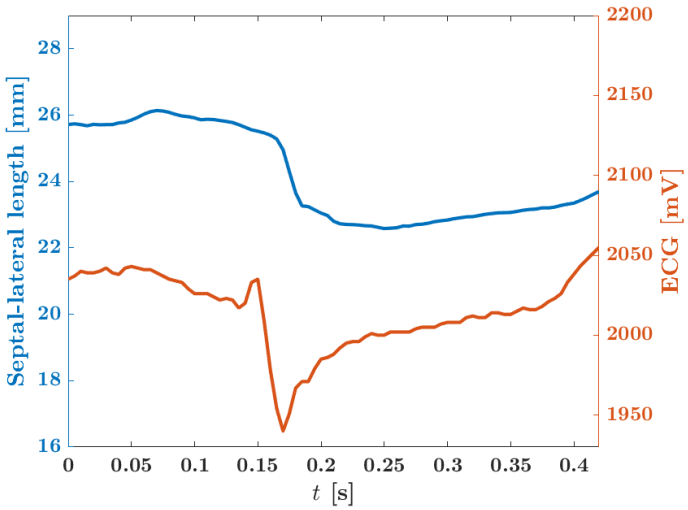

Figure 5.12: The SL observed during the relevant sections of the cardiac cycle. The SL has been shown with a blue line. The ECG curve (orange) serves as a reference.

5.3 FEM modelling of the mitral valve apparatus

5.3.1 Mesh refinement study

In order to make a suitable and justified choice of mesh size for subsequent use of dynamic BCs, a mesh refinement study was performed on the FEM model using static BCs. A total of 6 different meshes with an increasing number of elements were investigated (see Table 5.1). The number of elements were increased by controlling the element seed, representing the approximate element size. An element size control of $^1/_2$ was used, indicating that the smallest element allowed was half the size of the largest element in the mesh.

The mid belly deflection of the AML was used to quantify the convergence of the mesh. $^{\Delta d}/_{d}$ in Table 5.1 has been defined as:

$$\frac{\mid d_n - d_{n-1} \mid}{d_n} \tag{5.1}$$

where d_n is defined as deflection the deflection corresponding to the nth refinement whereas d_{n-1} follows as the deflection corresponding to the previous refinement.

The element showed a clear tendency of convergence with increasing number of elements. However, the results should be interpreted with caution, as the refined mesh required addition and repositioning of multiple chordae tendineae along the free edge of the MV leaflets. The mesh refinement therefore *altered* the geometry in some sense, indicating that the results should not be used blindly. Any further mesh refinements were not possible to stabilize numerically.

Table 5.1: An overview of the mesh refinement scheme.The S4 element was analyzed using 6 different element seeds. The mid belly deflection of the AML was used as a measure of convergence, which criterion has been given by Equation 5.1.

Element type	Element seed [mm]	# elements	d [mm]	$\Delta d/d$ [-]
S4	6.00	110	4.91	-
	3.00	195	5.95	0.175
	1.50	595	6.18	0.036
	1.25	955	6.43	0.039
	1.00	1482	6.48	0.006
	0.75	2503	6.53	0.008

For visualization purposes, the deflection was plotted against the corresponding number of elements (see Figure 5.13). A converging trend was observed. According to Table 5.1, the relative residual given by Equation 5.1 was in the per mille-range for the two last refinements, strongly indicating a converged solution.

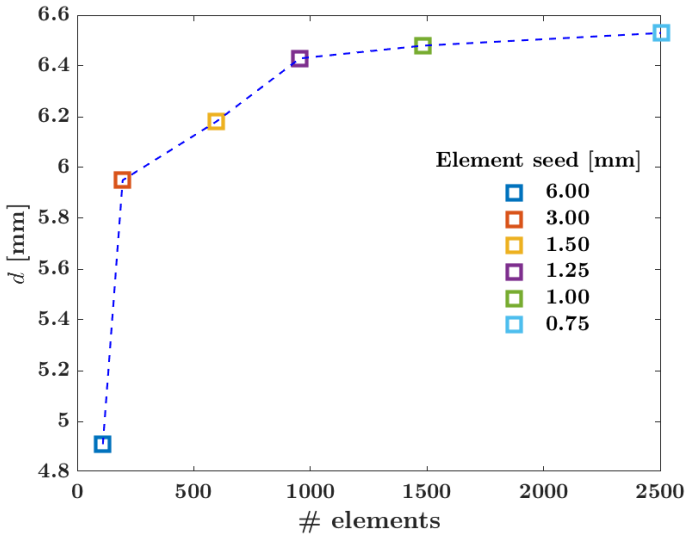

Figure 5.13: The mid belly deflection of the AML plotted against the corresponding number of S4 elements. The discrete squares represent the different element seeds investigated, respectively. The dotted blue line represent a linearly interpolated solution.

5.3.2 FEM modelling using static boundary conditions

Allowing for later comparison, the MV dynamics were simulated using static BCs in ABAQUS/Explicit [67].

Closure of the mitral valve leaflets

Using static BCs, no MR could be observed (see Figure 5.14). Four hallmark configurations are shown in the figure: The reference configuration, end diastole, peak

systole and end systole. Their corresponding pressure loads have been denoted in the figure. Please note that the thickness of the MV leaflets have not been rendered. No leakage was documented in the peak and end systolic configurations.

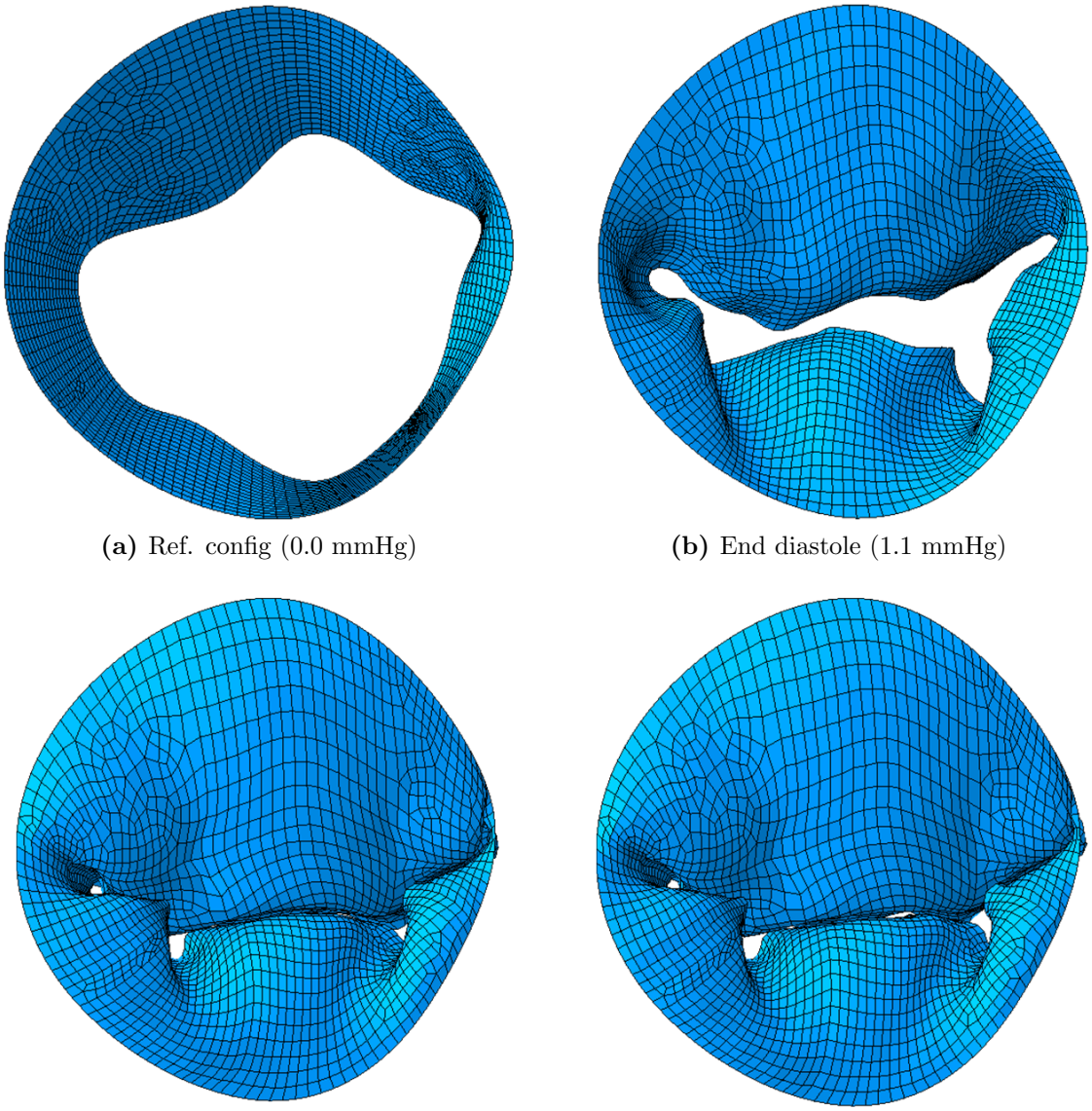

(a) Ref. config (0.0 mmHg)

(b) End diastole (1.1 mmHg)

(c) Peak systole (69.2 mmHg)

(d) End systole (28.3 mmHg)

Figure 5.14: Four configurations of the MV leaflets using static BCs ((a) Ref. config; (b) End diastole; (c) Peak systole; (d) End systole)

Papillary muscle forces

The magnitude of the total force vector of each papillary muscle group was recorded during a load cycle (see Figure 5.15). The AL group was predominantly heavier load than the PM group. The AL group reached a global maxima of 2.83 N after 0.269 s, before decreased in a nonlinear fashion to an end value of 1.17 N. The PM group reached its global maxima of 1.62 N after 0.281 s. Thereafter, it decreased with the same trend as the AL group, reaching an end value of 0.68 N.

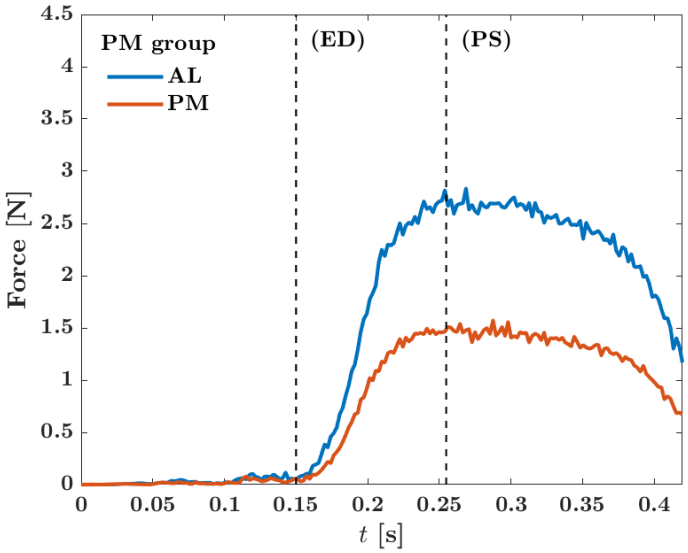

Figure 5.15: The magnitude of the total force vector of each papillary muscle group extracted from the nodal values in ABAQUS/Explicit using static BCs. The blue line represents the AL group, whereas the orange line represents the PM group. The instances of end diastole (ED) and peak systole (PS) have been indicated in dotted vertical lines. The AL group was found predominantly heavier loaded than the PM group.

Contact area

The total contact area of the MV leaflets was extracted from ABAQUS/Explicit for later comparison of the closure of the MV (see Figure 5.16). The contact area increased rapidly as the pressure load increased. A global maxima of 225.9 mm^2 was reached after 0.290 s, occurring immediately after peak systole (indicated with dotted vertical line). The area then decreased in a stepwise fashion, reaching an end value of 157.9 mm^2.

Furthermore, the contact area was normalized against the total initial area of the MV geometry. The initial area was extracted from the geometric model in ABAQUS/Explicit, and was found to be 1111.0 mm^2. The maximum normalized area then followed as 20.3% (see Figure 5.16).

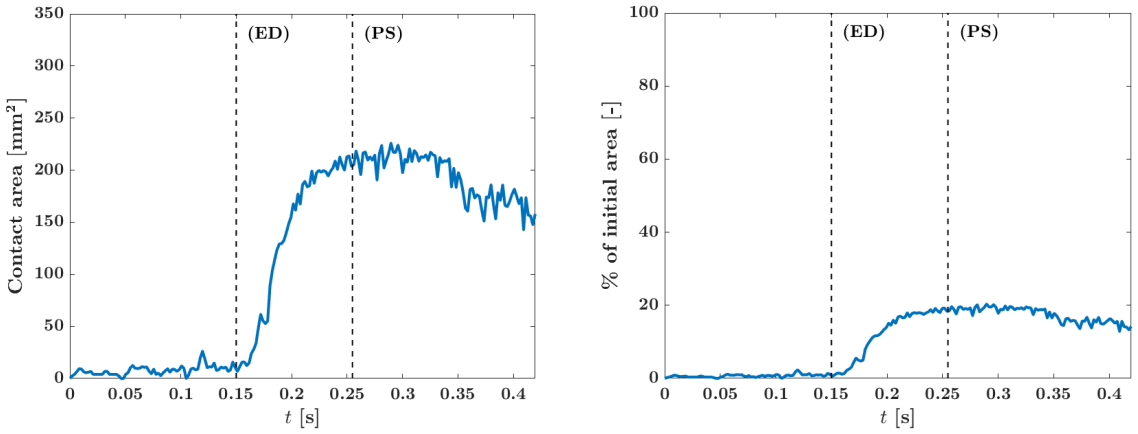

(a) Contact area **(b)** Normalized contact area

Figure 5.16: The contact area of the MV leaflets measured in ABAQUS/Explicit using static BCs ((a); Contact area (b); Normalized contact area). The instances of end diastole (ED) and peak systole (PS) have been indicated in dotted vertical lines. The contact area increased rapidly as the pressure load was applied, reaching a global maxima of 225.9 mm^2 after 0.290 s. The corresponding normalized area was 20.3%

5.3.3 Preliminary FEM modelling using dynamic boundary conditions

Thereafter, the BCs were modified to follow a prescribed deformation pattern enforced by the user subroutine VDISP in ABQUS/Explicit (see section 4.1.10).

Papillary muscle forces with initial placement of chordae tendineae

As with the static BCs, the papillary muscle forces were extracted from each group respectively (see Figure 5.17). The AL group force steadily increased to a local maxima of 6.64 N after 0.210 s. Some oscillatory behaviour were observed towards end systole, followed by an abrupt increase to a global maxima and end value of 82.31 N. The PM group force rapidly peaked to a global maxima of 456.99 N at 0.149 s. An additional peak occured towards end systole, reaching a value of 308.84 N.

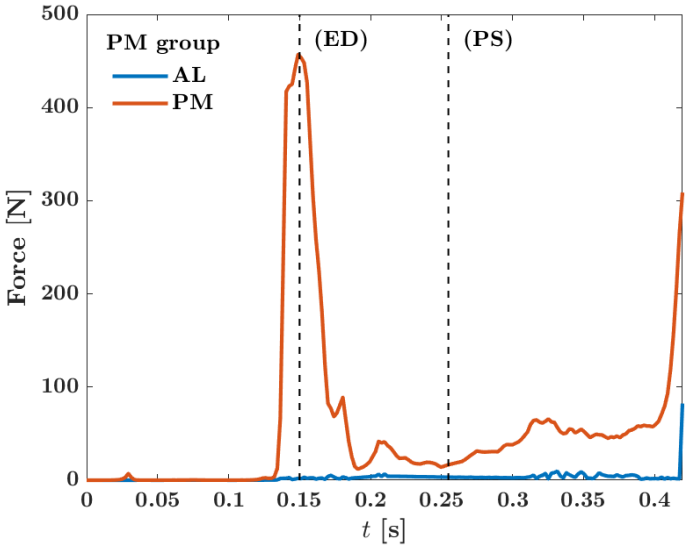

Figure 5.17: The magnitude of the total force vector of each papillary muscle group using dynamic BCs prescribed by user subroutines. The blue line represents the AL group, whereas the orange line represents the PM group. The instances of end diastole (ED) and peak systole (PS) have been indicated with dotted vertical lines.

Contact area with initial placement of chordae tendineae

The total contact area increased when using dynamic BCs (see Figure 5.18). The contact area increased vastly following the increased pressure load, reaching a plateau level of about 250 mm^2 after peak systole. The global maxima of 267.7 mm^2 was reached after 0.344 s. The contact area ultimately decreased rapidly to an end value of 82.2 mm^2. Notably, the contact area remained at its plateau value much longer than its static counterpart.

When normalized against the total initial area of the MV leaflets, the maximum contacting surface rendered 24.1% (see Figure 5.18b).

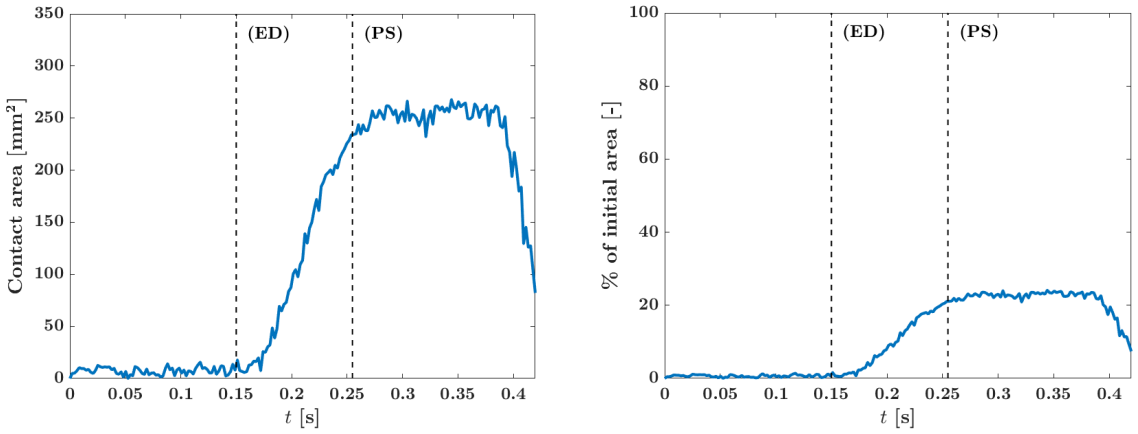

(a) Contact area **(b)** Normalized contact area

Figure 5.18: The contact area of the MV leaflets measured in ABAQUS/Explicit using dynamic BCs ((a); Contact area (b); Normalized contact area). The instances of end diastole (ED) and peak systole (PS) have been indicated in dotted vertical lines. The maximum contact area of 267.7 mm^2 occurred after 0.344 s. The corresponding normalized value was 24.1%.

5.3.4 Improved FEM modelling using dynamic boundary conditions

In an attempt to avoid the significant peaks of the papillary muscle forces seen in section 5.3.3, the positioning of the chordae tendineae was modified to increase the crimp of the fibers. Thus, without altering the papillary muscle dynamics, the stresses were expected to decrease.

Closure of the mitral valve leaflets

Using dynamic BC conditions, a small regurgitative region could be observed near the transition between the P2-A2 and P3-A3 segments (see section 3.3.1) in the peak and end systolic configurations (see Figure 5.19). Four hallmark configurations are shown in the figure: The reference configuration, end diastole, peak systole and end systole. Their corresponding pressure loads have been denoted in the figure. Please note that the thickness of the MV leaflets have not been rendered.

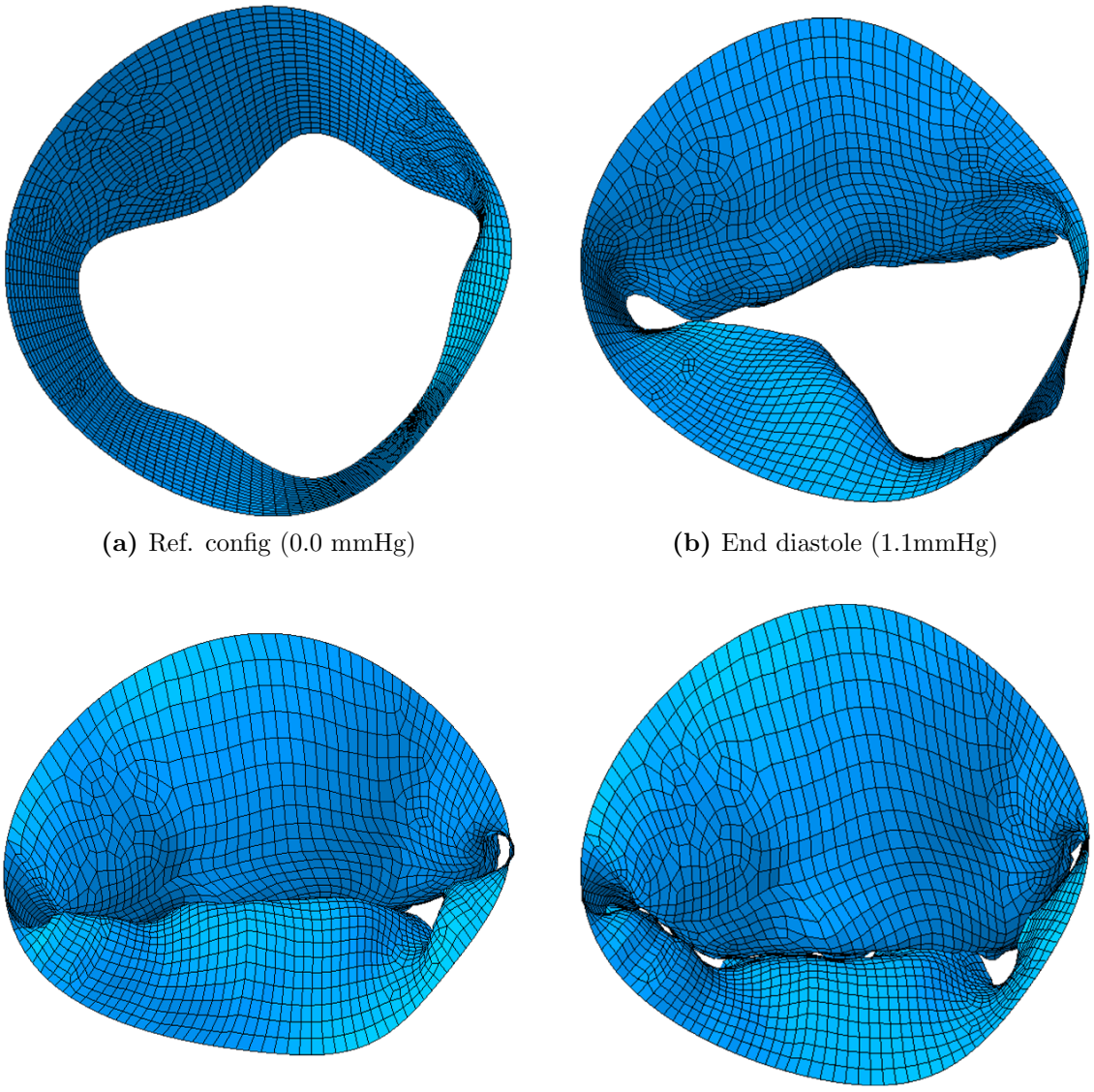

(a) Ref. config (0.0 mmHg)

(b) End diastole (1.1mmHg)

(c) Peak systole (69.2 mmHg)

(d) End systole (28.3 mmHg)

Figure 5.19: Four configurations of the MV leaflets using dynamic BCs and improved chordae positioning ((a) Ref. config; (b) End diastole; (c) Peak systole; (d) End systole)

Papillary muscle forces using improved configuration

The papillary muscle forces were significantly reduced as an effect of the repositioned chordae tendineae (see Figure 5.20). Both groups were nearly identical until end diastole. Thereafter, the AL group was consistently heavier loaded until peak systole. The AL group reached a maximum value of 3.89 N after 0.216 s. Thereafter, the load decreased with nearly constant rate to an end value of 1.41 N. The PM group reached a local maxima of 2.96 N in early systole (0.208 s), before some oscillatory behaviour was observed through systole. A maximum value of 4.12 N was reached in late systole (0.388 s). Ultimately, the force decreased abruptly to an end value of 2.56 N.

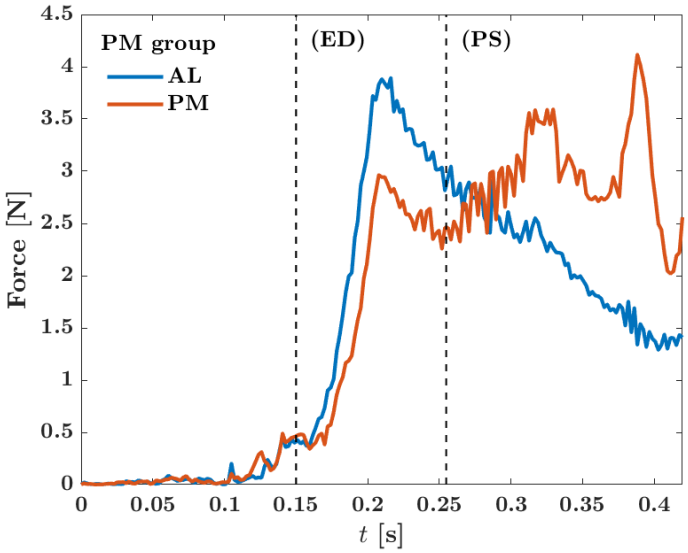

Figure 5.20: The magnitude of the total force vector of each papillary muscle group measured using ABAQUS/Explicit using dynamic BCs and an improved reference configuration with increased initial length of the chordae tendineae. The blue line represents the AL group, whereas the orange line represents the PM group. The instances of end diastole (ED) and peak systole (PS) have been indicated with dotted vertical lines.

Contact area using improved configuration

The contact area of the MV leaflets increased significantly by improving the initial configuration (see Figure 5.21). The peak systolic contact area was found to be in the same range as in the first configuration of the chordae tendineae. Notably, the increasing trend thereafter continued into late systole, where it reached a global maxima of 329.0 mm^2 after 0.336 s. The contact area then decreased to a final value of 164.5 mm^2 in end systole.

The corresponding maximum normalized area equaled 29.6% (see Figure 5.21).

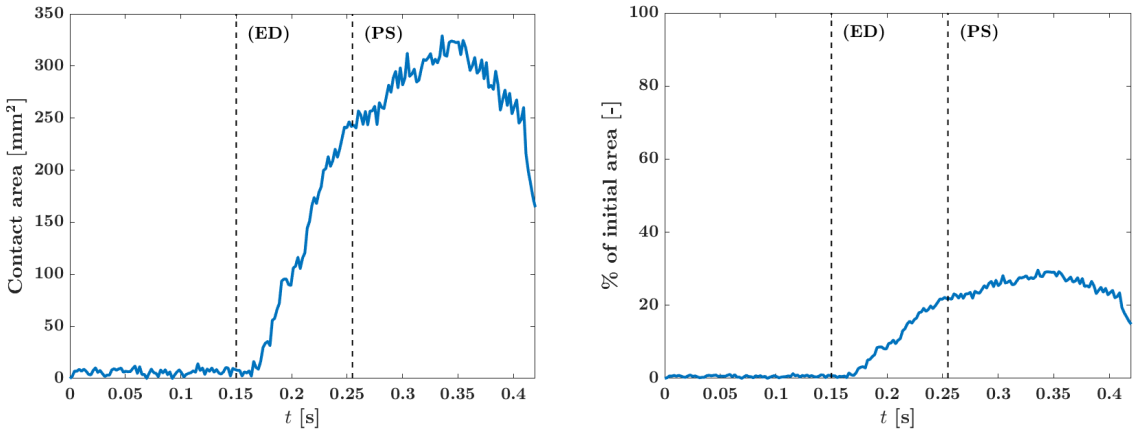

(a) Contact area **(b)** Normalized contact area

Figure 5.21: The contact area of the MV leaflets measured in ABAQUS/Explicit using dynamic BCs and an improved reference configuration with increased initial length of the chordae tendineae. ((a); Contact area (b); Normalized contact area). The instances of end diastole (ED) and peak systole (PS) have been indicated in dotted vertical lines. The contact area reached a global maxima of 329.0 mm^2 after 0.336 s. The corresponding normalized area was 29.6%.

Peak systolic principal strains

In order to investigate the local deformation field of the MV leaflets, the maximum absolute in-plane true strain field was extracted in the peak systolic configuration (see Figure 5.22a).

The mid belly-region of the AML was found to be under true tensile strains up to 75%. Furthermore, the regions near the commissures were in fact under true *compressive* strains close to -100%. Discontinuities in the strain field was observed in some of the transitions between changing material orientation. The direction of the peak systolic principle strains were mainly perpendicular to the MA in the mid belly region for both the AML and PML, whereas the tendency near the commissures was a principle strain direction parallel to the MA (see Figure 5.22b).

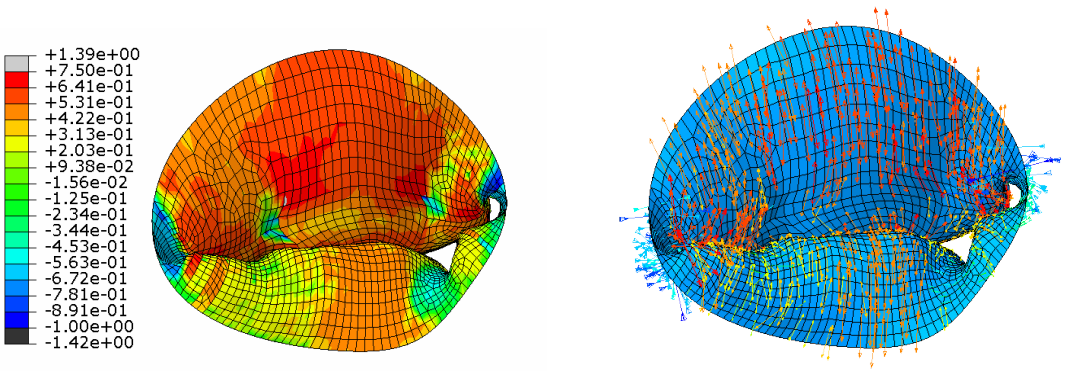

(a) Principal strain field **(b)** Direction of principal strains

Figure 5.22: The peak systolic absolute principle strain field obtained using dynamic BCs in ABAQUS/Explicit. Upper tensile cut-off boundary was set to 0.75, whereas the compressive limit was set to -1.00.

Peak systolic stresses

The von Mises stress field of the MV leaflets were extracted in the peak systolic configuration (see Figure 5.23). A large region of stresses up to 1.00 MPa could be observed in the mid-belly region of the AML. The remaining sections of the MV leaflets were loaded below stresses of 0.50 MPa. A few stress extremitites could be observed with stresses reaching values above the cut-off value of 2.00 MPa. Furthermore, the directions of the maximum principle stresses were observed to reflect the material orientation presented in section 4.1.12 well (see Figure 5.24).

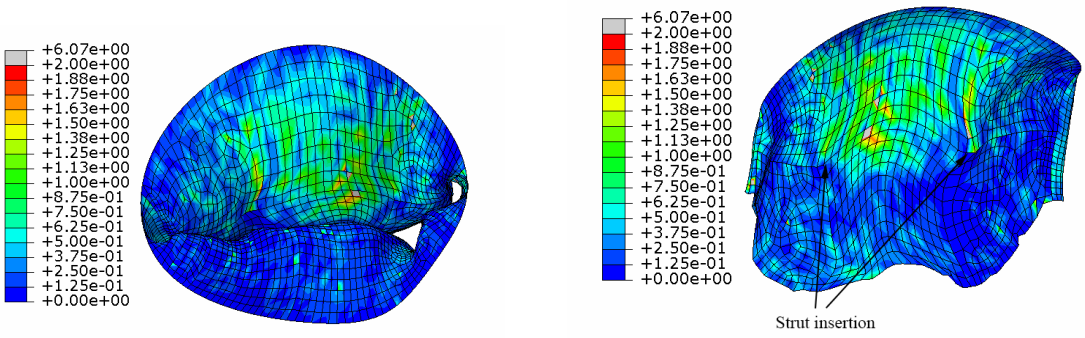

(a) Atrial view **(b)** Anterior leaflet from ventricular view

Figure 5.23: The von Mises stresses [MPa] in peak systole obtained using dynamic BCs in ABAQUS/Explicit.

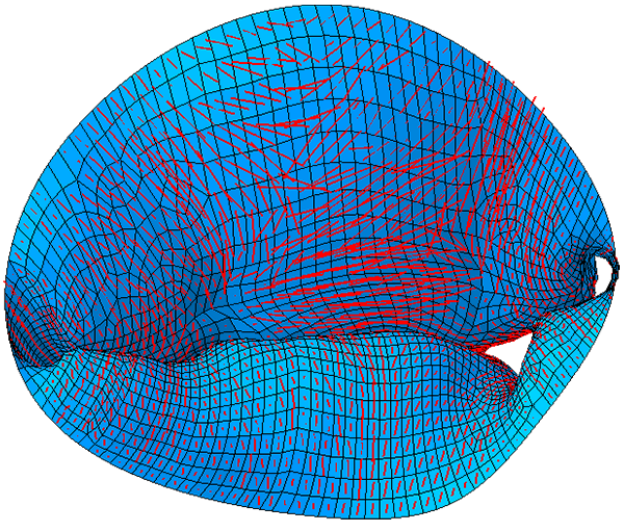

Figure 5.24: Directions of the maximal principle stresses using dynamic BCs in ABAQUS/Explicit.

Annular forces

The forces acting on the different sections of the MA was investigated in end diastole, peak systole and end systole, respectively. Devoid of any prestrain, the reference configuration rendered stress-free, and was therefore omitted from the analysis.

In its end-diastolic configuration, the force vectors were directed in the atrial direction (see Figure 5.25). The magnitudes of the force vectors revealed that the MA was heavier loaded near the commissure sections (2-3 and 6-7, see Table 5.2). In comparison, the nearby sections sustained loads nearly an order of magnitude *smaller* (3-4 and 7-8).

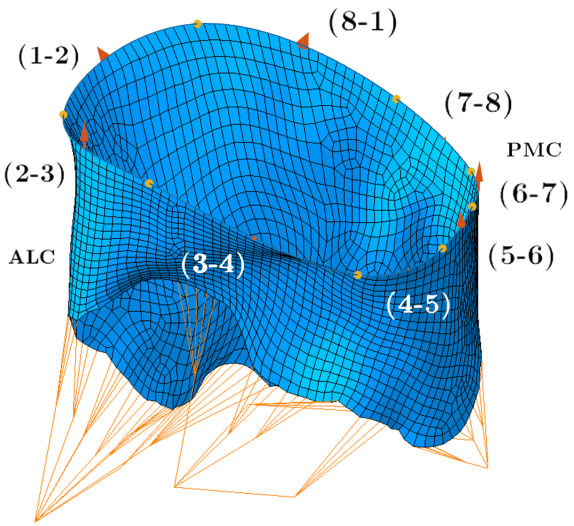

Figure 5.25: The sectionally averaged force vectors acting on the MA (orange arrows) in its end diastolic configuration shown between the respective crystals (yellow dots). NOTE: The force vectors have been scaled by a factor of 10 for visualization purposes.

Table 5.2: An overview of the magnitudes of the force vectors acting between two subsequent crystals in end diastole.

Section	$\lvert \bar{F} \rvert$ [N]
1-2	0.11
2-3	0.22
3-4	0.05
4-5	0.02
5-6	0.16
6-7	0.22
7-8	0.03
8-1	0.12

The forces vastly increased in peak systole (see Figure 5.26). Notably, most sections were loaded radially in the direction of the atrioventricular orifice. The anterior sections (1-2 and 8-1) were more than an order of magnitude heavier loaded in comparison to their end diastolic load (see Table 5.3). The same could be observed for section 3-4 and 4-5 on the PML, indicating that the dilative stresses on the MA increased in peak systole.

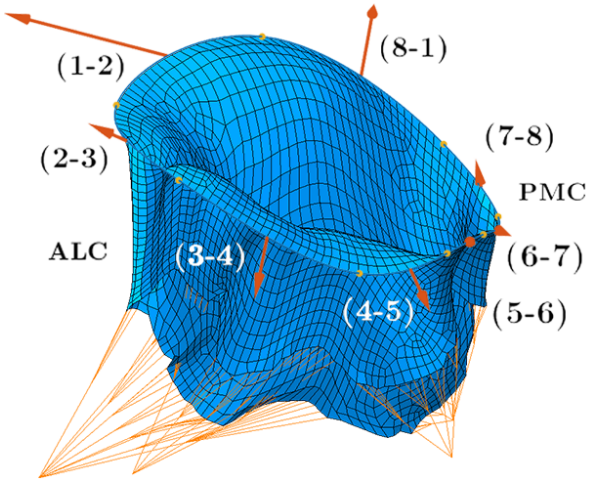

Figure 5.26: The sectionally averaged force vectors acting on the MA (orange arrows) in its peak systolic configuration shown between the respective crystals (yellow dots). NOTE: The force vectors have been scaled by a factor of 10 for visualization purposes.

Table 5.3: An overview of the magnitudes of the force vectors acting between two subsequent crystals in peak systole.

Section	$\lvert \bar{F} \rvert$ [N]
1-2	1.29
2-3	0.32
3-4	0.48
4-5	0.47
5-6	0.23
6-7	0.23
7-8	0.23
8-1	1.35

The load on the region near the PMC increased significantly in the end systolic configuration (see Figure 5.27). Furthermore, the direction of the load was once again pointing in the atrial direction. The direction of the load on the anterior sections (1-2 and 8-1) and the posterior sections (3-4 and 4-5) was maintained in end systole, although the magnitude of the load was greatly reduced.

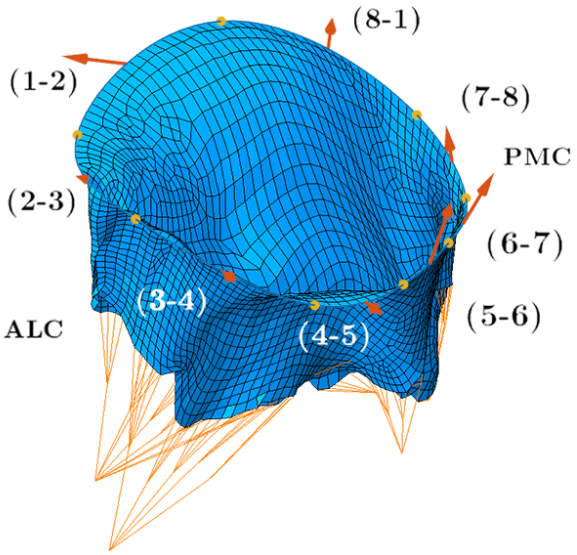

Figure 5.27: The sectionally averaged force vectors acting on the MA (orange arrows) in its end systolic configuration shown between the respective crystals (yellow dots). NOTE: The force vectors have been scaled by a factor of 10 for visualization purposes.

Table 5.4: An overview of the magnitudes of the force vectors acting between two subsequent crystals in end systole.

Section	$\lvert \bar{\mathbf{F}} \rvert$ [N]
1-2	0.52
2-3	0.09
3-4	0.40
4-5	0.35
5-6	0.97
6-7	0.49
7-8	0.30
8-1	0.47

5.3.5 FEM modelling using modified dynamic boundary conditions

The model was then modified in order to quantify the impact of AC on the MV dynamics.

Modification of annular dynamics

In order to investigate the effects of AC, the MA dynamics in the relevant sections of the cardic cycle were modified. As discussed in section 5.2, a distinct local maxima could be observed in all measures of MA dynamics following AC.

It was decided to neglect these effect by *locking* the MA in its pre-maximal configuration area wise, thus avoiding the dynamic effects of AC (see Figure 5.28). The area of the MA was thus forced to stay constant until the instance corresponding to the local maxima in early systole (shown in dotted red), contrary to the original path with a distinct peak (shown in dotted blue). In order to avoid discontinuities in the deformation field, the MA was thereafter linearly interpolated into its configuration at $t = 0.199s$ (shown with a declined, dotted red line).

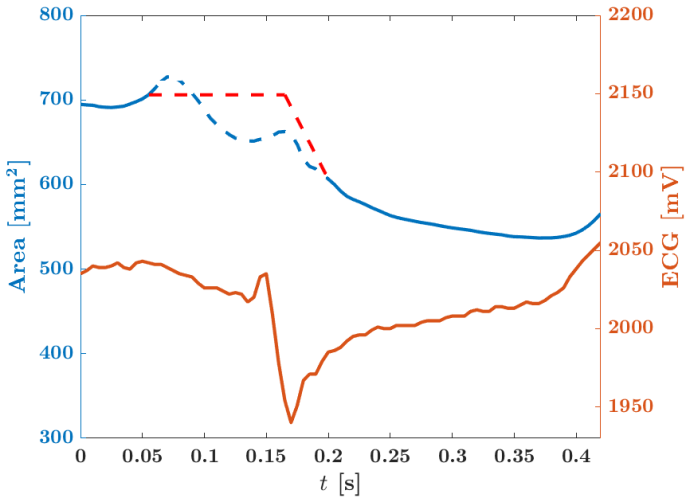

Figure 5.28: The modification of the MA BCs. The original path through atrial systole into early ventricular systole is shown in dotted blue. The modified path is shown in dotted red, indicating that the MA configuration was locked until early systole, before a linear interpolation into the current configuration was performed.

Closure of the mitral valve leaflets using modified boundary conditions

A small regurgitating region could be observed near the transition between the P2-A2 and P3-A3 segments in the peak and end systolic configurations as the modified BCs were introduced (see Figure 5.29). Notably, this was also observed for the previous analysis using unmodified BCs. Four hallmark configurations are shown in the figure: The reference configuration, end diastole, peak systole and end systole. Their corresponding pressure loads have been denoted in the figure. Please note that the thickness of the MV leaflets have not been rendered.

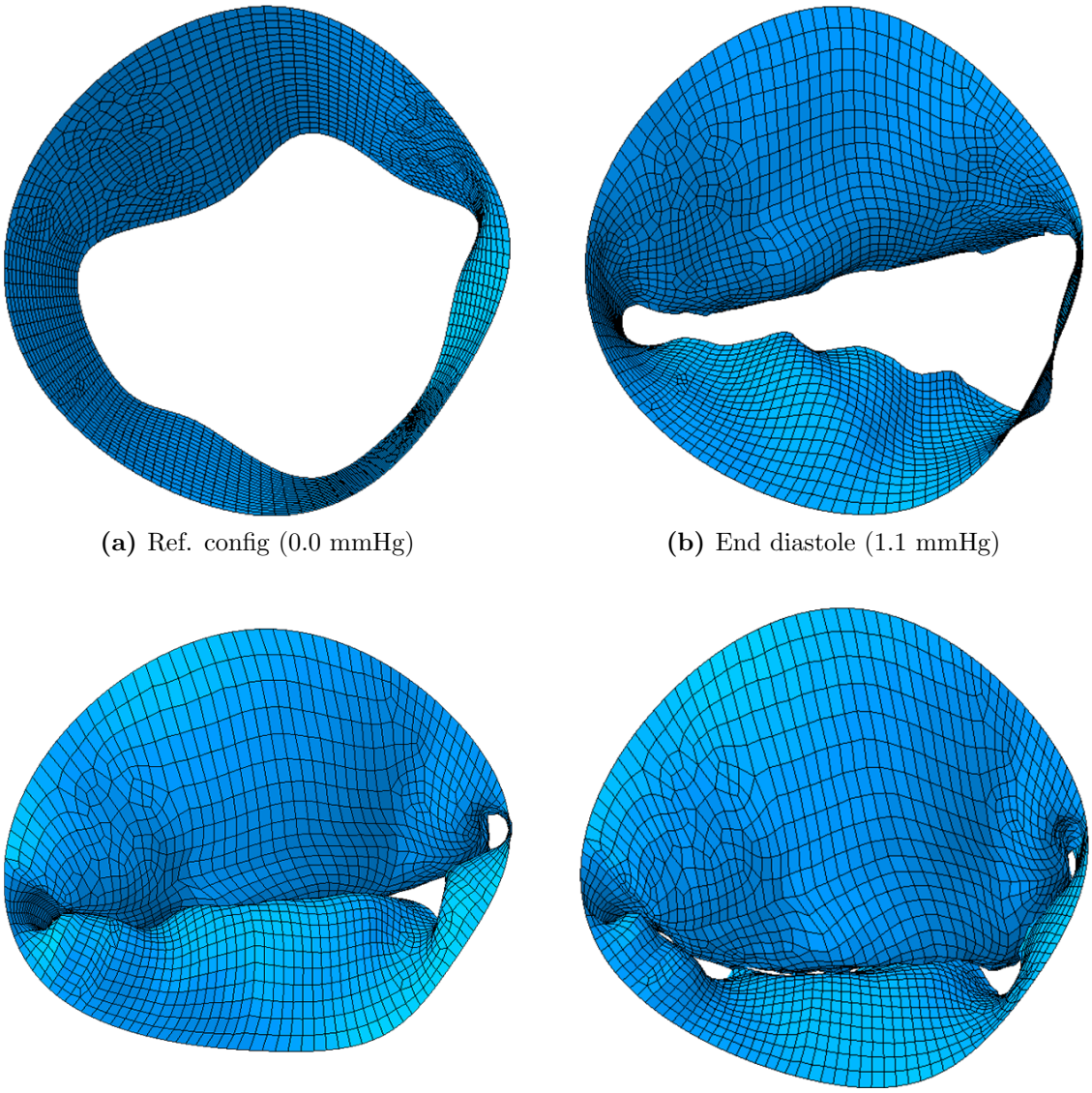

(a) Ref. config (0.0 mmHg)

(b) End diastole (1.1 mmHg)

(c) Peak systole (69.2 mmHg)

(d) End systole (28.3 mmHg)

Figure 5.29: Four configurations of the MV leaflets using modified dynamic BCs ((a) Ref. config; (b) End diastole; (c) Peak systole; (d) End systole)

Papillary muscle forces using modified boundary conditions

The papillary muscle forces followed a trend similar to the forces observed using unmodified boundary conditions. However, a distinct peak of 1.94 N was observed for the PM group near ED. Thereafter, the PM group was merely heavier loaded compared to its unmodified counterpart until the end of the modified section. The maximum force of 4.04 N occurred after 0.390 s, compared to the 4.12 N found previously. The end value was 2.56 N, identical to unmodified configuration.

The maximum load on the AL group was 4.04 N, in contrast to 3.89 N found using the unmodified setup. Thereafter, the same nearly constant decrease followed. The load in end systole was 1.39 N, compared to 1.41 N found previously.

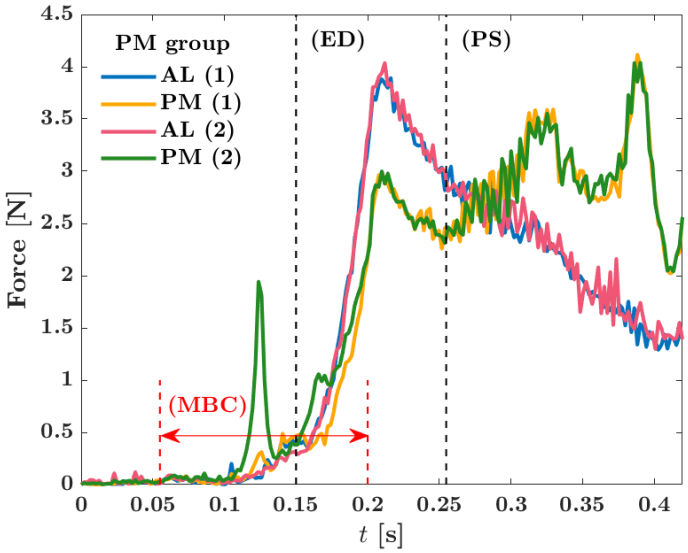

Figure 5.30: The magnitude of the total force vector of each PM group measured using ABAQUS/Explicit using modified dynamic BCs. The AL force corresponding to the unmodified (1) and modified (2) BCs have been plotted with blue and pink lines, respectively. Likewise, the PM force have been plotted in yellow and green lines, corresponding to the unmodified (1) and modified (2) BCs. The instances of end diastole (ED) and peak systole (PS) have been indicated with dotted vertical lines. The section with modified BCs (MBC) have been indicated with dotted red lines.

Contact area using modified boundary conditions

The contact area was nearly identical between the two configurations until peak systole (see Figure 5.31). Thereafter, increase in the the modified contact area declined, reaching a plateau level below the unmodified curve. The unmodified configuration continued to increase into late systole. The maximum area reached by the modified configuration was 296.6 mm^2, obtained at nearly the identical timeframe in late systole as the previous maximum value of 329.0 mm^2. A distinct local minima of 192.2 mm^2 could be observed in late systole. The end value of the modified and unmodified configuration was 143.9 mm^2 and 164.5 mm^2, respectively.

The corresponding maximum normalized contact areas followed as 26.7% and 29.6% for the modified and unmodified configuration respectively.

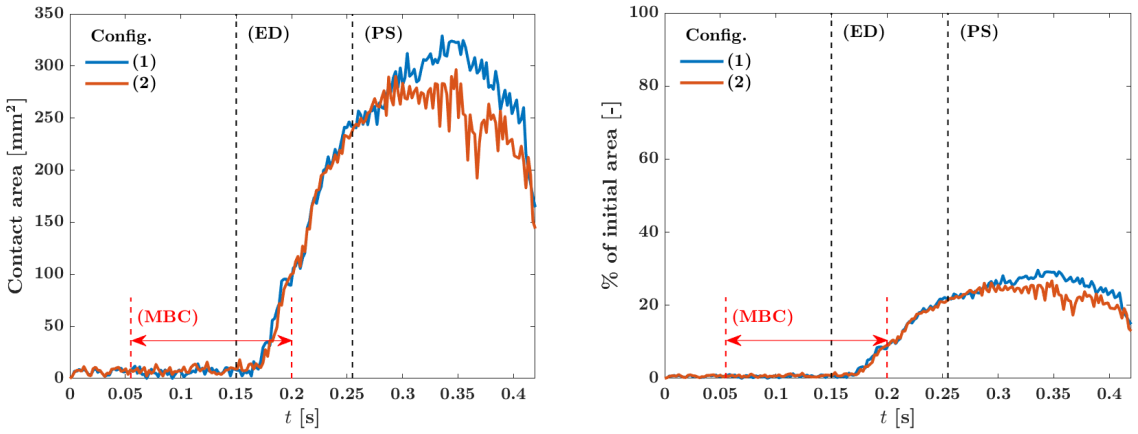

(a) Contact area **(b)** Normalized contact area

Figure 5.31: The contact area of the MV leaflets measured in ABAQUS/Explicit using modified dynamic BCs. ((a); Contact area (b); Normalized contact area). The instances of end diastole (ED) and peak systole (PS) have been indicated in dotted vertical lines. The section with modified MCs (MBC) have been indicated with dotted red lines. The unmodified (1) and modified (2) contact area have been plotted with blue and orange lines, respectively. The maximum modified area was 296.6 mm^2, whereas the maximum unmodified area was 329.0 mm^2. The corresponding maximum normalized areas were 26.7% and 29.6%.

Peak systolic principal strains using modified boundary conditions

The maximum absolute in-plane principle true strain field in the peak systolic configuration showed a similar deformation pattern to the unmodified configuration (see Figure 5.32a). The true tensile strains in the mid-belly region of the AML were again observed to be near 75%, whereas the regions near the commissures were under true compressive strains near -100%.

Regarding the directions of the principle strains, they were as for the unmodified configuration observed to be mainly perpendicular to the MA in the mid-belly regions of both MV leaflets (see Figure 5.32b). Near the commissural regions, the directions of the principle strains tended to be parallel to the MA.

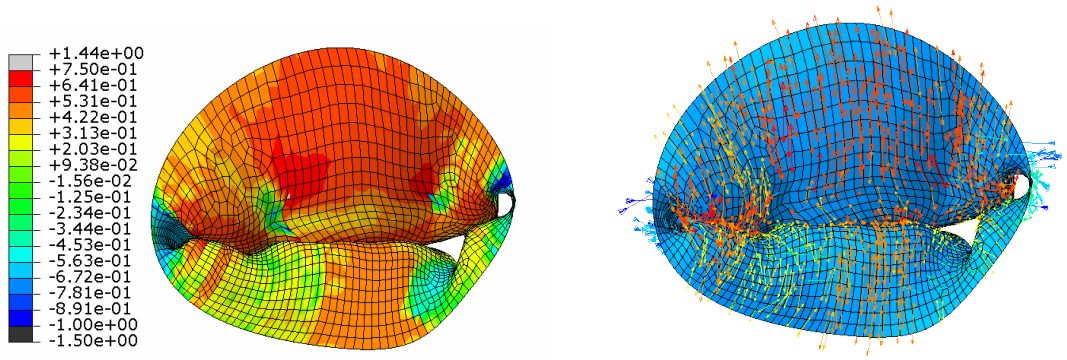

(a) **(b)**

Figure 5.32: The peak systolic absolute principle strain field obtained using modified dynamic BCs in ABAQUS/Explicit. Upper tensile cut-off boundary was set to 0.75, whereas the compressive limit was set to -1.00.

Peak systolic stresses using modified boundary conditions

Similar for the analysis with an unmodified MA BC, the von Mises stress field in the peak systolic configuration showed stresses up to around 1.00 MPa in the mid-belly region of the AML. The high stress region was observed to be sparser compared to the previous configuration. Furthermore, stress extremities exceeding the cut-off value of 2.00 MPa was observed near the strut insertion points (see Figure 5.33). The direction of the principle stresses reflected the assigned material orientation presented in section 4.1.12 well (see Figure 5.34).

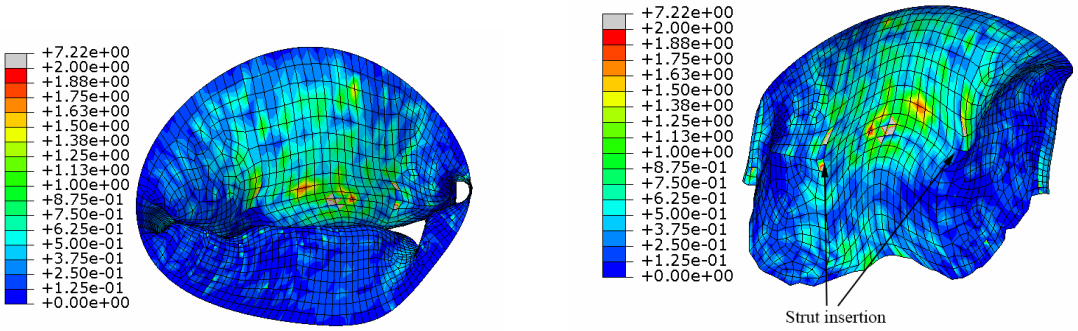

(a) Atrial view. **(b)** Anterior leaflet from ventricular view.

Figure 5.33: The von Mises stresses [MPa] in peak systole obtained using modified dynamic BC in ABAQUS/Explicit.

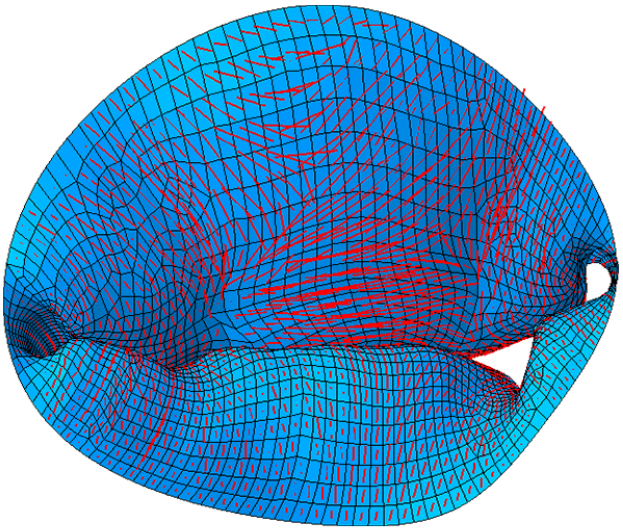

Figure 5.34: Directions of the maximal principle stresses using modified dynamic BC in ABAQUS/Explicit.

Annular forces using modified boundary conditions

The forces acting on the MA were found as explained in section 5.3.4.

As with the unmodified BCs, the MA forces were predominantly directed towards the LA in the end diastolic configuration (see Figure 5.35). Furthermore, the commissure sections were loaded heavier than the remaining sections, although the corresponding amplitudes were reduced by around 50% compared to their unmodified counterparts.

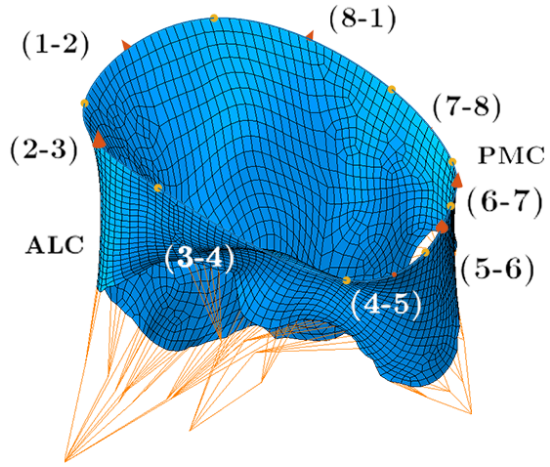

Figure 5.35: The sectionally averaged force vectors acting on the MA (orange arrows) in its end diastolic configuration shown between the respective crystals (yellow dots). The MA BC have been modified to assess the effects of AC. NOTE: The force vectors have been scaled by a factor of 10 for visualization purposes.

Table 5.5: An overview of the magnitudes of the force vectors acting between two subsequent crystals in end diastole.

Section	$\lvert \bar{\mathbf{F}} \rvert$ [N]
1-2	0.09
2-3	0.14
3-4	0.02
4-5	0.05
5-6	0.13
6-7	0.12
7-8	0.02
8-1	0.09

Except for the force vector near the PMC, the force vectors were directed in the radial direction towards the atrioventricular orifice in the peak systolic configuration (see Figure 5.36). Notably, the same trend could be observed for the unmodified configuration. Moreover, the forces along the anterior sections (1-2 and 8-1) were found oppositely directed to the forces along the posterior sections (3-4 and 4-5).

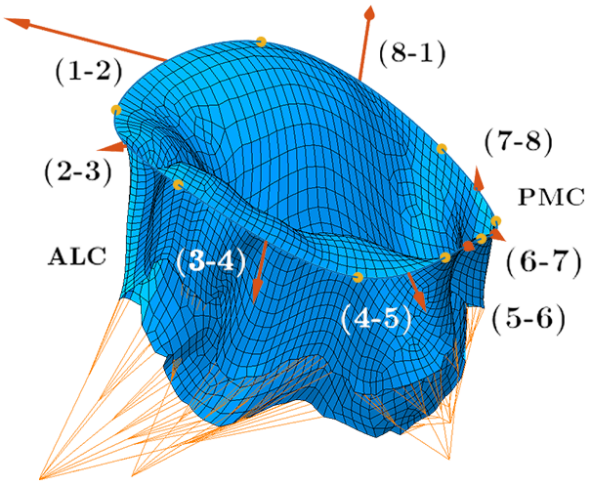

Figure 5.36: The sectionally averaged force vectors acting on the MA (orange arrows) in its peak systolic configuration shown between the respective crystals (yellow dots). The MA BC have been modified to assess the effects of AC. NOTE: The force vectors have been scaled by a factor of 10 for visualization purposes

Table 5.6: An overview of the magnitudes of the force vectors acting between two subsequent crystals in peak systole.

Section	$\lvert \bar{\mathbf{F}} \rvert$ [N]
1-2	1.28
2-3	0.23
3-4	0.51
4-5	0.44
5-6	0.22
6-7	0.20
7-8	0.23
8-1	1.39

The load on section 5-6 and 6-7 increased significantly relative to their peak systolic magnitude (342.5% and 176.4%, respectively). Furthermore, the corresponding force vectors were directed towards the LA. Meanwhile, the load magnitude on section 1-2 and 8-1 was reduced by 55.5% and 64.0% relative to their peak systolic magnitudes. The directions of the corresponding force vectors were similar to those seen in the peak systolic configuration.

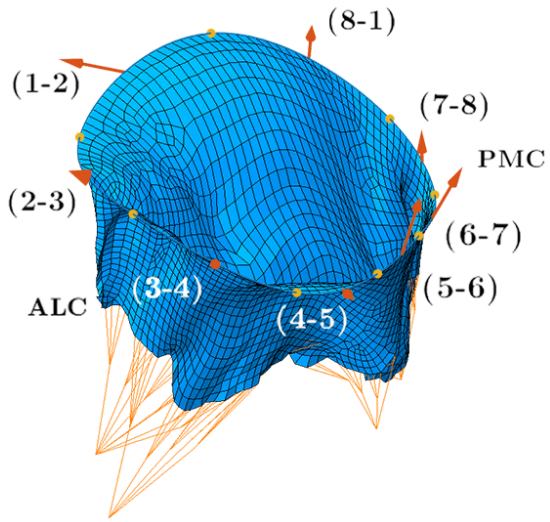

Figure 5.37: The sectionally averaged force vectors acting on the MA (orange arrows) in its end systolic configuration shown between the respective crystals (yellow dots). The MA BC have been modified to assess the effects of AC. NOTE: The force vectors have been scaled by a factor of 10 for visualization purposes

Table 5.7: An overview of the magnitudes of the force vectors acting between two subsequent crystals in end systole.

Section	$\lvert \bar{\mathbf{F}} \rvert$ **[N]**
1-2	0.57
2-3	0.16
3-4	0.32
4-5	0.31
5-6	0.98
6-7	0.56
7-8	0.28
8-1	0.50

6. Discussion

In this study, the effects of AC on the MV dynamics have been studied by developing a hyperelastic FEM-model in correspondence with dynamic BCs. Initially, the incompressibility of the chosen element type was numerically verified by comparing with an analytical test case. Furthermore, the dynamics of two different coordinate systems were assessed and related, which relation was found to affect all subsequent analyses.

A suitable mesh size was chosen based on a convergence study using static BCs. Thereafter, the FEM-analysis was conducted with increasing complexity with respect to BCs: Firstly, the MV apparatus was evaluated using static BCs. Thereafter, dynamic BCs were prescribed, resulting in very high papillary muscle forces. The initial length of the chordae tendineae was therefore modified for all subsequent analyses. Ultimately, the effects of AC were investigated by modifying the MA BC. The results have been discussed in detail below.

6.1 Residual effects in the reference configuration

As mentioned in section 4.1.1, prestrains were not taken into account in this model. However, residual strains have been known to exist in biological tissues for several decades [73, 74]. Regarding the MV apparatus, a study conducted by Amini *et al.* reported that the excision of the MV from an exsanguinated heart resulted in 18% and 30% circumferential and radial contraction respectively, indicating the existence of substantial residual strains [75].

It is important to keep in mind that the constitutive model used in this study was based on *ex vivo* data [11]. It is concluded that an implementation of prestrains in this model is necessary to reflect the *in vivo* state of the MV apparatus better, as further verified in recent computational studies [76, 77, 78].

6.2 Modification of the load curve

The LVP was measured using a manometer-tipped catheter [13]. However, no information regarding the atrioventricular pressure gradient or the LA pressure was

available in the given data set. As the atrioventricular pressure gradient can be assumed to be very small during mid diastole, the initial LVP was subtracted from the entire load curve in order to correct for the LA pressure. This does not render correct in a physiological sense, as the LA pressure is known to vary in a cyclic fashion. Although the variation in LA pressure is known to be very small relative to the LVP, information regarding its variation should be attained in order to fully comprehend the pressure load on the MV apparatus. [19]

6.3 Transformation of coordinates

Transformation of coordinates between the two local coordinate systems proved to be a difficult task based on several assumptions. First and foremost, the base vectors in both systems were generated based on an optimized plane of the MA geometry (see section 4.1.5). The first in-plane base vector relied on manual location of the anterior horn in the US recordings, introducing errors in the order of magnitude of a few degrees. This eventually lead to the US frame being incorrectly oriented with respect to the crystal frame.

Furthermore, the MA dynamics in the two systems where found to be very different, as the US MA showed much larger displacements through a cardiac cycle (see Figure 5.6). It is therefore questionable whether the approach of using an optimized plane as an aid of transforming points was suitable in this particular case, as it remains unknown whether this method was able to capture the orientation of the MA correctly.

However, it should be noted that only vectors *relative* to the local MA plane were transformed, supporting the chosen method as the different nature of the two systems was avoided (see section 4.1.5). Ultimately, the only way to avoid transformation of papillary muscle motion through an entire cardiac cycle would be to suture crystals the papillary muscles as well, which should be conducted in future studies.

6.4 Fitting of ECG-points

In order to take motion of the papillary muscles into account, manual identification of instances in the two different ECGs was necessary. Out of 18 discrete ultrasound recordings available in the time interval of interest, only 12 could be identified as corresponding instances in the crystal ECG (see Figure 4.8). Notably, the two cycles were of *different length*, indicating that the ultrasound measurements did not represent an identical cycle. It should therefore be questioned whether the two data sets can be said to be corresponding. Furthermore, the crystal ECG recordings were rather coarse, complicating the manual location of hallmark wave points.

6.5 Regarding the assumption on constant thickness

As noted in section 4.1.14, the thickness of each leaflet was assumed to be constant. However, this does not render correct in a physiological sense. Both histological and computational studies have confirmed that the thickness varies between the MA and the free edge of the MV leaflets [76, 79]. Ideally, the thickness should have been been assigned more smoothly in order to obtain more realistic results. Under the assumption of constant thickness, the stiffness of the region near the MA and free edge have been under- and overestimated, respectively.

6.6 Image quality of the ultrasound recordings

A crucial step of obtaining an accurate geometrical model of the MV leaflets was the quality of the US recordings data. For the data set used in this study, the image quality was found to be of mediocre quality. In order to increase the reliability of the results, US recordings with higher image quality should be made.

6.7 Verification of incompressibility

As shown in section 4.3.2, the incompressibility condition from Equation 4.4 was satisfied for all element seeds. This strongly supports that the S4 element can be assumed to be incompressible when used in correspondence with the built-in hyperelastic material models in ABAQUS/Explicit [67].

Regarding the calculation of stresses, the deviations observed for larger mesh sizes are *expected*, as the material model used was stretch based (see Table 4.5). For coarser mesh sizes, the stretch and thus stresses of the elements approximating the arc in Figure 4.11 are underestimated.

6.8 Physiological state of the porcine heart

It is suspected that the physiological state of the studied heart was altered following the suturing of the crystals. The procedure involved opening of the pericardium (for a explanation of the different layers of the heart, see section 3.1) and an incision through all layers of the LA heart wall, potentially introducing residual strains in the heart wall [13].

Independent studies have concluded that the apex can be assumed to be a fixed point [80, 81]. However, in this study, the apex was found to undergo large motion, as the distance between the extremal points rendered more than 15 mm (see Figure 5.1).

However, regarding the normally projected distance from apex, the distinct peak found in the crystal system are in line with results from previous studies (see Figure 5.4) [80]. Although the peak distance occurred somewhat *later* than expected, a decreasing trend could be observed through late systole. Moreover, the results from the US measurements derailed distinctively, as the distance to the apex in fact increased in the systolic phase (see Figure 5.7).

Furthermore, the peculiar MA dynamics following suturing of the crystals supports the possibility of an altered physiological configuration of the heart (see Figure 5.3). The rather unexpected distinct lateral motion that occurred with a dynamic origin could not be identified in the US recordings, which also used a dynamic origin (see Figure 5.6).

6.9 Quality of the mitral annulus boundary

It became evident that the crystal MA dynamics were altered when the apex motion was taken into account (see Figure 5.2 and Figure 5.3). Compared to the crystal MA dynamics obtained using a static origin, the motion showed a clear lateral tendency as the origin was modified to follow the apex motion. Notably, a gradual rotation of the MA plane was observed during the relevant sections of the cardiac cycle. According to literature, these are not attributes that describe a normal functioning MA, where the MA dynamics have been found to be devoid of any rotation [12, 41].

Therefore, it was decided that the MA dynamics referred to a *static* origin were to constitute the BCs of the FEM model. The MA dynamical results obtained with this boundary comply well with findings in literature (see section 5.2). Notably, the CW increased during early systole, whereas the SL decreased substantially (see Figure 5.11 & Figure 5.12). Consequently, the non-planarity of the MA increased as previously demonstrated in computational studies [82].

Furthermore, the perimeter was observed to decrease until end systole relative to the reference configuration (see Figure 5.10). This reflects that the MA was mostly under compressive strains in these sections of the cardiac cycle well [41].

6.10 Closure of the mitral valve leaflets

The closure of the MV leaflets was found highly sensitive to the positioning of the chordae tendineae and type of BCs. Using static boundary conditions, no significant regurgitation could be observed (see Figure 5.14). However, the contacting area was observed to be lower than what was later achieved using dynamic BCs.

Although the contact area increased more than 18.5% relative to the static contact area as the dynamic BCs with preliminary chordae positioning were introduced, the regurgitation was observed to increase (see Figure 5.18a). Evident from Figure 5.17, the chordae tendineae were stressed significantly, hindering a full coaptation of the

MV leaflets near the commissures.

The influence of the chordae tendineae became evident as their initial length was modified. The contact area increased 45.6% relative to the static contact area (see Figure 5.21). Furthermore, the regurgitation was observed to decrease, as the deformation constraint on the free edge of the MV leaflets was relaxed following the modification of the chordae tendineae.

Ultimately, the contact area decreased as the effects of AC were neglected (see Figure 5.31). Compared to the static contact area, the relative increase was 31.3%. The consequental changes from the unmodified configuration were revealed in late systole, as the contact area started to decrease nearly directly after peak systole.

It became evident that the model was prone to late coaptation of the MV leaflets. Full coaptation occurred *after* peak systole for all configurations. It is suspected that this phenomenon was related to the papillary muscle motion, as their motion after peak systole aided an increased coaptation.

6.11 Papillary muscle forces and influence of the chordae tendineae

It became evident from the use of static BCs that the papillary muscles were unevenly loaded, ultimately reported for all subsequent configurations. Except for the erroneous results obtained in section 5.3.3, the maximum load on each group was nearly identical in all subsequent configurations. However, the *instances* at which the maximum load occurred for each group were completely different (see Figure 5.20 and Figure 5.30). These results are in strong disagreement with previous findings, which have indicated an even load distribution between the two papillary muscle groups throughout the cardiac cycle [32].

Namely, the maximum load on the PM group was expected to occur simultaneously as that of the AL group in peak systole. These findings must be viewed in context of the great uncertainty of the papillary muscle motion. As noted previously, no US recordings were performed during the QRS-complex. Moreover, the late-systolic behaviour of the US MA plane deviated distinctively from the behaviour of the crystal MA, potentially affecting the transformation of the motion.

Furthermore, the PM group was consistently observed closer to the free edge of the MV leaflets than its AL counterpart, contradictive to previous *ex vivo* studies of the MV apparatus [33].

The effect of initial crimp in the chordae tendineae became evident in this study. Approximated as straight rod elements, the degree of crimp could be adjusted by varying the initial length of the elements. Ultimately, the stress in the chordae tendineae was drastically reduced following an elongation of the initial length. Effectively, the papillary muscle force amplitude where found to be fully in line with *in vitro* studies on porcine hearts [32].

A possible solution regarding the sensitivity to the user-defined initial crimp could be to attain more information from the US recordings. Moreover, the chordae tendineae were modelled using two-noded truss elements, the only truss element available in ABAQUS/Explicit while conducting this study. With only two nodes available, the deformation field was assumed to be constant. In future studies, a mesh refinement using the current element type or an implementation of higher-order elements should be conducted in order to better approximate the *in vivo* state of the chordae tendineae.

6.12 Principal strains

Large tensile strains was observed in the mid belly regions for both configurations of the MA. Furthermore, the direction of the principal strain was perpendicular to the local material direction in these regions, reflecting previous findings from *in vitro* studies on porcine hearts well [83]. According to the same study performed by Sacks *et al.*, it is apparent that the current work over-estimates the magnitude of the principal strains in the mid belly regions. Whereas the *in vitro* results reported maximum principal strain values of 34%, the current study reached values above 53% in the corresponding regions of the MV leaflets.

Furthermore, the current study was unable to reflect the circumferential strains along the free edges reported in previous *in vitro* studies on ovine hearts[66, 76, 78]. These findings are suspected to be correlated to the positioning of the papillary muscles, which favoured radial strains along the free edges in the current study due to their apical motion in systole.

Local variations in the strain field was observed near the insertion sites of the strut chordae, as reported in previous FEM modeling the MV apparatus [77]. Indeed, a finer mesh in these regions could be employed to avoid large gradients between adjacent elements.

6.13 Principal stress

In the configuration where AC was taken into account, the von Mises stress in the mid belly region of the AML was distinctively larger than the remaining regions of the MV apparatus. In fact, the stress in this region was found to be around 1.00 MPa, although some stress extremities could be observed. In the remaining regions, the von Mises stress was observed to be lower than 0.50 MPa.

The von Mises stress field of the second configuration shared strong similarities with the first configuration. The mid belly stresses were around 1.00 MPa, apart from some stress extremities closer to the free edge. Notably, the high stress regions were more sparse than previously found.

Compared to previous computational studies done on the MV apparatus, this model

shows a larger range in terms of stress. In a study performed by Dal Pan *et al.* on the human MV, the maximum von Mises stress was found to be 0.345 MPa [84]. Furthermore, results obtained by Prot *et al.* on a porcine heart reported stresses in the mid belly region of the AML consistenly lower than 0.472 MPa [82]. However, it is important to keep in mind that several factors, most notably the material model and leaflet thickness, will inherently affect the stresses. Therefore, a comparison of the results should be done with caution.

It is suspected that the unexpectedly large stresses obtained with the current model occurred due to the intricate motion of the boundary conditions. As the distance between MA plane and papillary muscle tips in fact *increased* in systole, the MV leaflets were put under excessive tension.

Interestingly, the direction of the principal stresses align with the implemented local material direction, as reflected by previous computational studies on the MV apparatus [77]. This shows the immense difference in stiffness between the material directions, as the principal stresses were observed to be orthogonally directed to the principal strains in the regions with large strains.

6.14 Annular forces

It became evident that the loading configuration of the MA changed significantly during a cardiac cycle. This yielded for both configurations of MA dynamics. Interestingly, the radial stresses increased substantially as the pressure load increased, indicating that the MA was under expansive stresses. Thus, these preliminary results reflect the lower stiffness of the posterior MA, expressed through lower force magnitudes.

It should be noted that certain sections of the MA were sensitive to the positioning of the chordae tendineae and the papillary muscle motion. More specifically, these effects exposed themselves near the PMC section, where the annular forces rotated distinctively into the atrial direction in end systole. This finding coincides well with the papillary muscle motion in the apical direction in the corresponding time interval.

6.15 Atrial contraction

To the authors' knowledge, this is the first time the effects of AC have been investigated using novel FEM-modelling. As presented in section 5.3.5, the effects of AC were neglected through a modification of the MA BCs. Based upon the advice of a leading cardiologist, it was decided to keep the MA area constant through atrial systole in order to simulate the absence of AC.

However, it should be mentioned that this was a mere approximation of the *in vivo* state of the heart absent of AC. It is suggested that the results of this study are

validated through the use crystal MA boundaries obtained in hearts absent of AC.

The contact area was observed to decrease relative to the unmodified configuration in late systole (see Figure 5.31). Compared to previous studies, it was difficult to predict the outcome of the absence of AC. As mentioned in section 3.3.5, a recent study conducted by Ito *et al.* concluded that a dilated MA in correspondence with a thethering of the PML due to enlargement of the LA could potentially reduce the coaptation of the MV leaflets [18]. However, the latter has not been evaluated in this study, and the results are therefore not directly comparable.

The findings in this study are reflected well by the study done by Tang *et al.*, where it was concluded that atrial dysfunction alone is *not sufficent* to generate MR on its own [44]. This is supported by previous studies on the topic, which suggested that the major role of AC is to augment the filling of the LV, not to prevent MR [85].

7. Conclusions

In this study, the influence of AC on MV closure mechanism was studied by developing a hyperelastic FEM-model of the MV apparatus. In hopes of increasing the reliability of the results, the MA BC was adapted from a previous *in vivo* study which used high-resolution crystals to obtain the MA dynamics [13]. Furthermore, the MV leaflets geometry as well the motion of the papillary muscles was generated from corresponding *in vivo* US recordings.

Compared to previously estimated *in vivo* results, the mechanical assessment of the MV apparatus indicated that the response of the structure as a whole was much softer than expected. This was largely devoted to the lack of prestrain in the model, leading to a strong discrepancy between the *ex vivo*-based material model and expected *in vivo* response. [77]

With respect to AC, the results obtained were able to reflect previous findings well, supporting that the absence of AC alone is not sufficient to generate MR [44]. In terms of stresses and strains, the two configurations of MA dynamics were hard to distinguish. To the authors' knowledge, this was the first time the effect of AC was assessed using FEM.

Eventually, it became evident that several sources of errors were introduced. First and foremost, the MA BC did not behave according to what one would expect from previous literature [41]. Secondly, the different nature of the crystal and US coordinate systems immediately questioned the validity of the results, as several quantities depended on a transformation between the systems. Thirdly, the quality of the US recordings hindered a precise location of the papillary muscles, eventually affecting the accuracy of the papillary muscle BC.

Furthermore, it should be pointed out that the results in this study have not been validated statistically. Due to the above-mentioned uncertainties, this is viewed as a strict necessity before the results can be stated to be of clinical significance.

8. Future outlooks

A troublesome element of this study was the extensive process of transforming coordinates between two dynamic coordinate systems. This could be avoided to a large extent if the papillary muscles BCs were recorded in the same system as the MA BC. Therefore, it is suggested that future *in vivo* clinical studies suture crystals to the PM tips as well in order to increase the validity of the results.

Furthermore, a method to incorporate the varying thickness of the MV leaflets should be implemented in the model. It is suggested that the thickness is mapped element wise either from US recordings or by generating a scalar field based on previous histological studies. A first measure should be to linearly interpolate the MV leaflet thickness between the MA and free edge.

Evidently, the positioning and initial length of the chordae tendineae was strongly affecting the end result. Therefore, a method of retrieving information regarding the *in vivo* initial state of the chordae tendineae should be implemented. It is suggested that high quality US recordings can be used for this purpose, ultimately increasing the validity of the results.

Bibliography

[1] S. Coffey, B. J. Cairns and B. Iung. "The modern epidemiology of heart valve disease". In: *Heart* 102.1 (2016), pp. 75–85.

[2] M. D. Seckeler and T. R. Hoke. "The worldwide epidemiology of acute rheumatic fever and rheumatic heart disease". eng. In: *Clinical epidemiology* 3 (2011), pp. 67–84.

[3] B. Remenyi, J. Carapetis, R. Wyber, K. Taubert and B. M. Mayosi. "Position statement of the World Heart Federation on the prevention and control of rheumatic heart disease". In: *Nature Reviews Cardiology* 10.5 (2013), pp. 284–292.

[4] V. T. Nkomo, J. M. Gardin, T. N. Skelton, J. S. Gottdiener, C. G. Scott and M. Enriquez-Sarano. "Burden of valvular heart diseases: a population-based study". In: *The Lancet* 368.9540 (2006), pp. 1005–1011.

[5] H. Gray. *Anatomy of the human body*. Bartleby, 2000.

[6] P. A. Iaizzo, ed. *Handbook of Cardiac Anatomy, Physiology, and Devices*. Springer International Publishing, 2015.

[7] R. A. Levine, M. D. Handschumacher, A. J. Sanfilippo, A. A. Hagege, P. Harrigan, J. E. Marshall and A. E. Weyman. "Three-dimensional echocardiographic reconstruction of the mitral valve, with implications for the diagnosis of mitral valve prolapse." In: *Circulation* 80.3 (1989), pp. 589–598.

[8] F. Maffessanti, P. Gripari, G. Pontone, D. Andreini, E. Bertella, S. Mushtaq, G. Tamborini, L. Fusini, M. Pepi and E. G. Caiani. "Three-dimensional dynamic assessment of tricuspid and mitral annuli using cardiovascular magnetic resonance". In: *European Heart Journal - Cardiovascular Imaging* 14.10 (2013), pp. 986–995.

[9] H. M. D. Aguilera, V. E. Prot, B. Skallerud and S. Urheim. "Finite element analysis of a Barlow mitral valve: patient specific geometry and comparison with three-dimensional echocardiographic data". In: *10th National Conference on Computational Mechanics MekIT'19*. 2019.

[10] G. A. Holzapfel, R. W. Ogden and S. Sherifova. "On fibre dispersion modelling of soft biological tissues: a review". In: *Proceedings of the Royal Society A: Mathematical, Physical and Engineering Sciences* 475.2224 (2019), pp. 1–22.

[11] K. M. Newman and F. C. Yin. "A constitutive law for mitral valve tissue". In: *Journal of Biomechanical Engineering* 120.1 (1998), pp. 38–47.

[12] C. E. Eckert, B. Zubiate, M. Vergnat, J. H. Gorman, R. C. Gorman and M. S. Sacks. "In vivo dynamic deformation of the mitral valve annulus". In: *Annals of Biomedical Engineering* 37.9 (2009), pp. 1757–1771.

[13] K.-A. Dumont, J.-P. E. Kvitting, J. S. Karlsen, E. W. Remme, J. Hausken, R. Lundblad, A. E. Fiane and S. Urheim. "Validation of a Holographic Display for Quantification of Mitral Annular Dynamics by Three-dimensional Echocardiography". In: *Journal of the American Society of Echocardiography* 32.2 (2019), 303–316.e4.

[14] S. Koneru et al. "Mitral valve disease—morphology and mechanisms". In: *The Annals of Thoracic Surgery* 12.3 (2016), pp. 689–710.

[15] A. Baumgarten. "Uber den Mechanismus, durch welchen die venosen Herzklapen geschlossen werden." In: *Archiv für Anatomie, Physiologie und wissenschaftliche Medicin* 463 (1843), pp. 463–471.

[16] R. C. Little. "The Mechanism of Closure of the Mitral Valve: A Continuing Controversy". In: *Circulation* 59.4 (1979), pp. 615–618.

[17] M. K. Chung, L. L. Eckhardt, L. Y. Chen, H. M. Ahmed, R. Gopinathannair, J. A. Joglar, P. A. Noseworthy, Q. R. Pack, P. Sanders and K. M. Trulock. "Lifestyle and Risk Factor Modification for Reduction of Atrial Fibrillation: A Scientific Statement from the American Heart Association". In: *Circulation* (2020), E750–E772.

[18] K. Ito, Y. Abe, Y. Takahashi, Y. Shimada, H. Fukumoto, Y. Matsumura, T. Naruko, T. Shibata, M. Yoshiyama and J. Yoshikawa. "Mechanism of atrial functional mitral regurgitation in patients with atrial fibrillation: A study using three-dimensional transesophageal echocardiography". In: *Journal of Cardiology* 70.6 (2017), pp. 584–590.

[19] R. E. Klabunde. *Cardiovascular Physiology Concepts*. Lippincott Williams & Wilkins, 2011. Chap. 4.

[20] S. K. Suvarna. *Cardiac Pathology*. Springer, Cham, 2019.

[21] M. Michail and A. J. Brown. "Physiology of the normal heart". In: *Medicine* 46.8 (2018), pp. 427–430.

[22] S. Shah, G. Gnanasegaran, J. Sundberg-Cohon and J. R. Buscombe. "The Heart: Anatomy, Physiology and Exercise Physiology". In: *Integrating Cardiology for Nuclear Medicine Physicians: A Guide to Nuclear Medicine Physicians*. Ed. by A. Movahed, G. Gnanasegaran, J. Buscombe and M. Hall. Berlin, Heidelberg: Springer Berlin Heidelberg, 2009, pp. 3–22.

[23] S.-x. Zhang. "Respiratory System". In: *An Atlas of Histology*. New York, NY: Springer New York, 1999, pp. 163–185.

[24] K. A. Eagle and R. B. Ragavendra. *Practical cardiology : evaluation and treatment of common cardiovascular disorders*. Lippincott Williams & Wilkins, 2003.

[25] J. D. Humphrey and A. D. McCulloch. "The Cardiovascular System — Anatomy, Physiology and Cell Biology". In: *Biomechanics of Soft Tissue in Cardiovascular Systems*. Ed. by G. A. Holzapfel and R. W. Ogden. Vienna: Springer Vienna, 2003, pp. 1–14.

[26] S. Y. Ho. “Anatomy of the mitral valve”. In: *British Heart Journal* 88.iv4 (2002), pp. iv5–iv10.

[27] K. P. McCarthy, L. Ring and B. S. Rana. “Anatomy of the mitral valve: understanding the mitral valve comoplex in mitral regurgitation”. In: *European Journal of Echocardiography* 11.10 (2010), pp. i3–i9.

[28] J. L. Quill, A. J. Hill, T. G. Laske, O. Alfieri and P. A. Iaizzo. “Mitral leaflet anatomy revisited”. In: *The Journal of Thoracic and Cardiovascular Surgery* 137.5 (2009), pp. 1077–1081.

[29] J. H. C. Lam, N. Ranganathan, E. D. Wigle and M. D. Silver. “Morphology of the Human Mitral Valve”. In: *Circulation* 41.3 (1970), pp. 449–458.

[30] S. R. Kaplan, G. Bashein, F. H. Sheehan, M. E. Legget, B. Munt, X.-N. Li, M. Sivarajan, E. L. Bolson, M. Zeppa, M. Arch and R. W. Martin. “Principles of Reconstructive Surgery in Degenerative Mitral Valve Disease”. In: *Seminars in Thoracic and Cardiovascular Surgery* 19.2 (2007), pp. 103–110.

[31] A. J. Sanfilippo, P. Harrigan, A. D. Popovic, A. E. Weyman and R. A. Levine. “Papillary muscle traction in mitral valve prolapse: Quantitation by two-dimensional echocardiography”. In: *Journal of the American College of Cardiology* 19.3 (1992), 564 LP –571.

[32] M. Ø. J. Jensen, A. A. Fontaine and A. P. Yoganathan. “Improved In Vitro Quantification of the Force Exerted by the Papillary Muscle on the Left Ventricular Wall: Three-Dimensional Force Vector Measurement System”. In: *Annals of Biomedical Engineering* 29.5 (2001), pp. 406–413.

[33] K. S. Kunzelman, R. P. Cochran, E. D. Verrier and R. C. Eberhart. “Anatomic Basis for Mitral Valve Modelling”. In: *The Journal of Heart Valve Disease* 3.5 (1994), pp. 491–6.

[34] A. Pozzoli, M. Zuber, M. Reisman, F. Maisano and M. Taramasso. “Comparative Anatomy of Mitral and Tricuspid Valve: What Can the Interventionlist Learn From the Surgeon”. In: *Frontiers in Cardiovascular Medicine* 5.80 (2018), pp. 1–9.

[35] H. Muresian. “The Clinical Anatomy of the Mitral Valve”. In: *Clinical Anatomy* 22 (2009), pp. 85–98.

[36] W. C. Roberts and J. K. Perloff. “A Clinicopathologic Survey of the Conditions Causing the Mitral Valve To Function Abnormally”. In: *Annals of Internal Medicine* 77 (1972), pp. 939–975.

[37] J. Ritchie, J. N. Warnock and A. P. Yoganathan. “Structural Characterization of the Chordae Tendineae in Native Porcine Mitral Valves”. In: *The Annals of Thoracic Surgery* 80.1 (2005), pp. 189–197.

[38] A. Angelini, S. Y. Ho, R. H. Anderson, M. J. Davies and A. E. Becker. “A histological study of the atrioventricular junction in hearts with normal and prolapsed leaflets of the mitral valve”. In: *British Heart Journal* 59.6 (1988), pp. 712–716.

[39] S. R. Kaplan, G. Bashein, F. H. Sheehan, M. E. Legget, B. Munt, X.-N. Li, M. Sivarajan, E. L. Bolson, M. Zeppa, M. Arch and R. W. Martin. "Three-dimensional echocardiographic assessment of annular shape changes in the normal and regurgitant mitral valve". In: *American Heart Journal* 139.3 (2000), pp. 378–387.

[40] J. J. Silbiger. "Anatomy, mechanics and pathophysiology of the mitral annulus". In: *American Heart Journal* 164.2 (2012), pp. 163–176.

[41] M. K. Rausch, W. Bothe, J.-P. E. Kvitting, J. C. Swanson, N. B. I. Jr., D. C. Miller and E. Kuhl. "Characterization of Mitral Valve Annular Dynamics in the Beating Heart". In: *Annals of Biomedical Engineering* 39.6 (2011), pp. 1690–1702.

[42] F. A. Flachskampf, S. Chandra, A. Gaddipatti, R. A. Levine, A. E. Weyman, W. Ameling, P. Hanrath and J. D. Thomas. "Analysis of Shape and Motion of the Mitral Annulus in Subjects With and Without Cardiomyopathy by Echocardiographic 3-Dimensional Reconstruction". In: *Journal of the American Society of Echocardiography* 13.4 (2000), pp. 277–287.

[43] J. K. Perloff and W. C. Roberts. "The Mitral Apparatus". In: *Circulation* 46.2 (1972), pp. 227–239.

[44] Z. Tang, Y. T. Fan, Y. Wang, C. N. Jin, K. W. Kwok and A. P. W. Lee. "Mitral Annular and Left Ventricular Dynamics in Atrial Functional Mitral Regurgitation: A Three-Dimensional and Speckle-Tracking Echocardiographic Study". In: *Journal of the American Society of Echocardiography* 32.4 (2019), pp. 503–513.

[45] M. Scott and I. Vesely. "Aortic valve cusp microstructure: The role of elastin". In: *The Annals of Thoracic Surgery* 60 (1995), S391–S394.

[46] L. D. Muiznieks and F. W. Keeley. "Molecular assembly and mechanical properties of the extracellular matrix: A fibrous protein perspective". In: *Biochimica et Biophysica Acta (BBA) - Molecular Basis of Disease* 1832.7 (2013), pp. 866–875.

[47] Y.-C. Fung. "Bioviscoelastic Solids". In: *Biomechanics: Mechanical Properties of Living Tissues*. New York, NY: Springer New York, 1993, pp. 242–320.

[48] "Collagen". In: *Tissue Mechanics*. Ed. by S. C. Cowin and S. B. Doty. New York, NY: Springer New York, 2007, pp. 289–339.

[49] N. Sasaki and S. Odajima. "Stress-strain curve and young's modulus of a collagen molecule as determined by the X-ray diffraction technique". In: *Journal of Biomechanics* 29.5 (1996), pp. 655–658.

[50] Sotirios Korossis. "Structure-Function Relationship of Heart Valves in Health and Disease". In: *Structural Insufficiency Anomalies in Cardiac Valves*. 2018. Chap. 1, pp. 1–37.

[51] C. M. Pollock and R. E. Shadwick. "Relationship between body mass and biomechanical properties of limb tendons in adult mammals". In: *American Journal of Physiology-Regulatory, Integrative and Comparative Physiology* 266.3 (1994), R1016–R1021.

[52] L. Debelle and A. M. Tamburro. "Elastin: molecular description and function". In: *The International Journal of Biochemistry & Cell Biology* 31.2 (1999), pp. 261–272.

[53] J. Gosline, M. Lillie, E. Carrington, P. Guerette, C. Ortlepp and K. Savage. "Elastic proteins: biological roles and mechanical properties". eng. In: *Philosophical transactions of the Royal Society of London. Series B, Biological sciences* 357.1418 (2002), pp. 121–132.

[54] G. A. Holzapfel. *Nonlinear Solid Mechanics*. Wiley, 2000.

[55] S. Ayoub, G. Ferrari, R. C. Gorman, J. H. Gorman III, F. J. Schoen and M. S. Sacks. "Heart Valve Biomechanics and Underlying Mechanobiology". In: *Comprehensive Physiology*. American Cancer Society, 2016, pp. 1743–1780.

[56] R. L. Leask, N. Jain and J. Butany. "Endothelium and valvular diseases of the heart". In: *Microscopy Research and Technique* 60.2 (2003), pp. 129–137.

[57] "Kinematics and Mechanics of Large Deformations". In: *Tissue Mechanics*. Ed. by S. C. Cowin and S. B. Doty. New York, NY: Springer New York, 2007, pp. 507–557.

[58] A. Spencer. *Deformation of Fibre-reinforced Materials*. Oxford Science Research Papers, 1972.

[59] Y. Feng, S. Qiu, X. Xia, S. Ji and C.-H. Lee. "A computational study of invariant I(5) in a nearly incompressible transversely isotropic model for white matter". eng. In: *Journal of biomechanics* 57 (2017), pp. 146–151.

[60] G. A. Holzapfel, T. C. Gasser and R. W. Ogden. "A new constitutive framework for arterial wall mechanics and a comparative study of material models". In: *Journal of Elasticity* 61.1-3 (2000), pp. 1–48.

[61] M. Smith. *ABAQUS User's Manual, Version 2017*. 2017. URL: `http://ivt-abaqusdoc.ivt.ntnu.no:2080/v6.14/books/usi/default.htm` (visited on 18/01/2020).

[62] A. Pokutta-Paskaleva, F. Sulejmani, M. DelRocini and W. Sun. "Comparative mechanical, morphological, and microstructural characterization of porcine mitral and tricuspid leaflets and chordae tendineae". In: *Acta Biomaterialia* 85 (2019), pp. 241–252.

[63] R. P. Cochran, K. S. Kunzelman, C. J. Chuong, M. S. Sacks and R. C. Eberhart. "Nondestructive analysis of mitral valve collagen fiber orientation". In: *ASAIO Transactions* 37.3 (1991), pp. M447–8.

[64] D. R. Einstein, K. S. Kunzelman, P. G. Reinhall, M. A. Nicosia and R. P. Cochran. "The relationship of normal and abnormal microstructural proliferation to the mitral valve closure sound". In: *Journal of Biomechanical Engineering* 127.1 (2005), pp. 134–147.

[65] Mathworks. *MATLAB R2019b*. 2019. URL: `se.mathworks.com`.

[66] M. K. Rausch, W. Bothe, J.-P. E. Kvitting, S. Göktepe, D. Craig Miller and E. Kuhl. "In vivo dynamic strains of the ovine anterior mitral valve leaflet". In: *Journal of Biomechanics* 44.6 (2011), pp. 1149–1157.

[67] Dassault Systemes. *ABAQUS/Explicit 2017*. 2017. URL: `https://www.3ds.com/products-services/simulia/products/abaqus/abaqusexplicit/`.

[68] *MATLAB Optimization Toolbox*. URL: https://se.mathworks.com/products/optimization.html (visited on 10/02/2020).

[69] Dassault Systèmes SolidWorks Corporation. *SOLIDWORKS 2019*. 2019. URL: https://www.solidworks.com/.

[70] R. D. Cook, D. S. Malkus, M. E. Plesha and R. J. Witt. *Concepts and applications of finite element analysis*. Fourth. John Wiley Sons Inc, 2001.

[71] A. Laulusa, O. A. Bauchau, J. Y. Choi, V. B. Tan and L. Li. "Evaluation of some shear deformable shell elements". In: *International Journal of Solids and Structures* 43.17 (2006), pp. 5033–5054.

[72] W. H. Press, S. A. Teukolsky, W. T. Vetterling and B. P. Flannery. *Numerical Recipes, The Art of Scientific Computing*. 3rd. Cambridge University Press, 2007.

[73] Y. C. Fung and S. Q. Liu. "Change of residual strains in arteries due to hypertrophy caused by aortic constriction." In: *Circulation Research* 65.5 (1989), pp. 1340–1349.

[74] Y. C. Fung. "What are the residual stresses doing in our blood vessels?" In: *Annals of Biomedical Engineering* 19.3 (1991), pp. 237–249.

[75] R. Amini, C. E. Eckert, K. Koomalsingh, J. McGarvey, M. Minakawa, J. H. Gorman, R. C. Gorman and M. S. Sacks. "On the in vivo deformation of the mitral valve anterior leaflet: Effects of annular geometry and referential configuration". In: *Annals of Biomedical Engineering* 40.7 (2012), pp. 1455–1467.

[76] M. K. Rausch, N. Famaey, T. O. Shultz, W. Bothe, D. C. Miller and E. Kuhl. "Mechanics of the mitral valve". In: *Biomechanics and Modeling in Mechanobiology* 12.5 (2013), pp. 1053–1071.

[77] V. Prot and B. Skallerud. "Contributions of prestrains, hyperelasticity, and muscle fiber activation on mitral valve systolic performance". In: *International Journal for Numerical Methods in Biomedical Engineering* 33.4 (2017), e2806 1–15.

[78] M. K. Rausch and E. Kuhl. "On the effect of prestrain and residual stress in thin biological membranes". In: *Journal of the Mechanics and Physics of Solids* 61.9 (2013), pp. 1955–1969.

[79] A. Itoh, G. Krishnamurthy, J. C. Swanson, D. B. Ennis, W. Bothe, E. Kuhl, M. Karlsson, L. R. Davis, D. C. Miller and N. B. Ingels. "Active stiffening of mitral valve leaflets in the beating heart". In: *American Journal of Physiology-Heart and Circulatory Physiology* 296.6 (2009), H1766–H1773.

[80] C. J. Jones, L. Raposo and D. G. Gibson. "Functional importance of the long axis dynamics of the human left ventricle." In: *Heart* 63.4 (1990), pp. 215–220.

[81] P. E. Assmann, C. J. Slager, S. T. Dreysse, S. G. van der Borden, J. A. Oomen and J. R. Roelandt. "Two-Dimensional Echocardiographic Analysis of the Dynamic Geometry of the Left Ventricle: The Basis for an Improved Model of Wall Motion". In: *Journal of the American Society of Echocardiography* 1.6 (1988), pp. 393–405.

[82] V. E. Prot, B. Skallerud and R. Haaverstad. “Finite element analysis of the mitral apparatus: annulus shape effect and chordal force distribution”. In: *Biomechanics and Modeling in Mechanobiology* 8 (2009), pp. 43–55.

[83] M. S. Sacks, Z. He, L. Baijens, S. Wanant, P. Shah, H. Sugimoto and A. P. Yoganathan. “Surface Strains in the Anterior Leaflet of the Functioning Mitral Valve”. In: *Annals of Biomedical Engineering* 30.10 (2002), pp. 1281–1290.

[84] F. Dal Pan, G. Donzella, C. Fucci and M. Schreiber. “Structural effects of an innovative surgical technique to repair heart valve defects”. In: *Journal of Biomechanics* 38.12 (2005), pp. 2460–2471.

[85] S. P. Nolan, S. H. Dixon, R. D. Fisher and A. G. Morrow. “The influence of atrial contraction and mitral valve mechanics on ventricular filling. A study of instantaneous mitral valve flow in vivo”. In: *American Heart Journal* 77.6 (1969), pp. 784–791.

Håvar Johan Junker and Vegar Tviberg

NTNU
Kunnskap for en bedre verden